Single-cell dynamics of genome-nucleolus interactions captured by nucleolar laser microdissection (NoLMseq)

Kaivalya Walavalkar[1], Shivani Gupta[1], Jelena Kresoja-Rakic[1], Mathieu Raingeval[1,2], Chiara Mungo[1,2], Raffaella Santoro[1]

1. Department of Molecular Mechanisms of Disease, DMMD, University of Zurich, Zurich, CH-8057, Switzerland
2. Molecular Life Science Program, Life Science Zurich Graduate School, University of Zurich, Zurich, CH-8057, Switzerland

*Corresponding author:
Raffaella Santoro (raffaella.santoro@dmmd.uzh.ch)

Abstract

Gene position in the nuclear space plays an important role in gene regulation. This is exemplified by repressive chromatin domains frequently contacting nuclear lamina or nucleoli. The nucleolus undergoes structural changes in response to various cellular states, potentially impacting genome organization. However, how the 3D-genome organization responds to nucleolar states has remained underinvestigated due to the lack of methods able to identify nucleolar associated domains (NADs) in single cells and under nucleolar stress. To address this, we developed NoLMseq, a method combining laser-capture microdissection and DNA sequencing to map NADs in single cells. NoLMseq identified many unexplored features of chromosome organization around single nucleoli such as NAD heterogeneity among ESCs, culminating in two major populations with distinct chromatin states. NADs prevalently contact nucleoli in a monoallelic manner and allelic nucleolar contact frequency mirrors gene expression and chromatin states. NoLMseq also revealed how chromosomes reorganise around nucleoli under nucleolar stress conditions, highlighting the importance of nucleolus integrity in genome organization and 3D-genome response to nucleolar stress. The results demonstrated that NoLMseq accurately measures chromosome contacts around single healthy and stressed nucleoli and it will be a critical tool to study NADs within biological populations and determine how the 3D-genome responds to nucleolar stress in healthy and disease states.

Introduction

The three-dimensional (3D) organization of chromosomes in the cell's nucleus plays an important role in the regulation of gene expression programs and cell fate. One important aspect of this regulation is the position of genes in the nuclear space. This is exemplified by the frequent location of repressive chromatin domains at the nuclear periphery (i.e., lamina associated domains, LADs) or around nucleoli (nucleolar associated domains, NADs) [1-3]. However, while LADs have extensively been studied in many cell types and in single cells, NADs have remained underinvestigated mainly due to technical limitations in identifying DNA sequences associating with a compartment lacking a membrane such as the nucleolus.

The nucleolus exhibits a highly dynamic structure that changes in response to external stimuli affecting ribosome biogenesis, a critical nucleolar process that is tightly regulated according to cell state [4]. These nucleolar structural alterations (i.e., size, number, or physico-chemical properties) might significantly impact the organization of the surrounding genome, thereby affecting gene expression and chromatin states. Ribosome biogenesis is initiated in the nucleolus by the RNA polymerase I (Pol I)-driven transcription of hundreds of ribosomal RNA (rRNA) genes (rDNA) that generate 45S/47S pre-rRNA. These transcripts are then modified, processed, and assembled with ribosomal proteins (RPs) in the nucleolus, forming pre-ribosomal particles [5]. rRNA genes are distributed among different chromosomes; acrocentric chromosomes in human cells and, in mouse cells, and depending on strain, they can generally be found at chromosomes 12, 16, 18, and 19 (rDNA-chromosomes) and close to centromeric regions [3]. Due to ribosome biogenesis, the nucleolus structure is influenced by cell states such that highly proliferative cells have larger nucleoli compared to quiescent cells [6-9]. Accordingly, alterations in nucleolar activities and structure have been well documented under many cellular stress conditions and in several diseases, such as cancer, neurodegenerative disorders, and premature ageing [10]. For example, nucleolar stress is defined as a condition in which abnormalities in nucleolar structure and function driven by diverse cellular insults, such as nutrient starvation or DNA damage, ultimately leads to activation of stress signalling pathways that downregulate ribosome biogenesis, including rRNA gene transcription, and alter nucleolar structure [11,12]. However, whether these structural alterations might have an impact on the genome organization around nucleoli remains unexplored, mainly due to technical limitations of current methods to map NADs.

67 Currently, there are several methods to identify NADs; the biochemical purification of nucleoli followed
68 by sequencing and, more recently, the Nucleolar-DamID that relies on the expression of an engineered
69 nucleolar histone H2B fused to Dam that serves to mark NADs with adenine methylation (H2B-Dam-
70 NoLS) and nucleolar-TSAseq [13,14]. Although based on different methodologies, these methods revealed
71 that NADs are composed of repressive chromatin domains [15-19]. However, these methods have also
72 some limitations. First, they cannot be applied to study how genome organization around nucleoli is
73 affected under nucleolar stress [20,21]. Indeed, under these conditions, nucleoli become frail and cannot
74 be efficiently biochemically purified. On the other side, the consequent downregulation of ribosome
75 biogenesis decreases protein translation, thereby affecting the expression of H2B-Dam-NoLS.
76 Moreover, the physico-chemical alterations of nucleoli upon rDNA downregulation causes the expulsion
77 of the H2B-Dam-NoLS from nucleoli similarly to other nucleolar components [19]. Finally, these methods
78 have only been applied in cell populations and consequentially they have provided an average nucleolar
79 contact frequency, which might not accurately reflect the structure of the genome around single nucleoli.
80 Thus, so far there is no methodology able to identify NADs under nucleolar stress conditions and in
81 single cells.
82 To overcome these challenges, we developed NoLMseq, a novel approach that combines laser-capture
83 microdissection (LCM) and DNA sequencing to identify NADs in single cells. LCM is a technique
84 traditionally used for isolating single cells or specific tissue regions[22-26] that we have expanded it for the
85 organelle-level isolation of single nucleoli. Traditional techniques to study genome organization
86 predominantly rely on either microscopy or DNA sequencing. NoLMseq synergistically integrates
87 strengths of both these approaches, enabling precise examination of the genome architecture
88 surrounding single nucleoli. The application of NoLMseq in mouse embryonic stem cells (ESCs) not
89 only confirmed the general repressive state of NADs but also provided novel insights of genome
90 organization around nucleoli that could not be detected in previous NAD studies since these were based
91 on methods that could only be applied in cell populations. These findings included the detection of
92 different levels of NAD heterogeneity among ESCs that culminates in two distinct cell populations with
93 distinct chromatin states, one more repressed than the other one. NoLMseq also determined that genes
94 detaching from nucleoli during ESC differentiation into neural progenitors are activated and linked to
95 neuronal pathways, implying an active role of the nucleolus in gene repression. Intriguingly, although
96 NADs are generally composed of repressive chromatin domains, NoLMseq detected a high frequency

97 association of the highly expressed ribosomal protein genes with the nucleolus. These findings indicate
98 that the repressive nucleolar compartment can also accommodate transcriptionally active genes and
99 suggest a potential direct role of nucleolar proximity in regulating ribosomal protein genes and,
100 consequently, ribosome biogenesis. Moreover, NoLMseq revealed that NADs prevalently contact
101 nucleoli in a monoallelic manner and that allelic nucleolar contact frequency correlates with gene
102 expression and chromatin states. Finally, we determined how genome structure is impacted under
103 conditions that impair nucleolar integrity, revealing the detachment of a substantial fraction of NADs
104 from nucleoli and their subsequent transcriptional activation. This insight, unattainable with previous
105 technologies, underscores the critical role of nucleolar integrity in genome organization and gene
106 expression, while also illuminating how the genome responds to nucleolar stress.
107 Together, these results not only provided novel insights of how chromosomes are organized around
108 nucleoli and their remodelling during cell fate commitment and stress-induced nucleolar structural
109 changes but also demonstrated that NoLMseq accurately measures chromosome contacts around
110 single healthy and "stressed" nucleoli. Thus, NoLMseq will be a critical tool to study NADs within
111 biological populations and determine how genome organization responds to nucleolar stress in healthy
112 and disease states.
113
114 **Results**
115 **NoLMseq identifies NADs in single cells**
116 To map NADs at a single nucleoli resolution, we combined laser-capture microdissection (LCM) of
117 nucleoli and DNA sequencing. We named this method nucleolus laser microdissection sequencing
118 (NoLMseq). We applied NoLMseq to mouse embryonic stem E14 cells (ESCs), thereby enabling
119 comparisons with NADs from ESC populations, which have recently been identified using Nucleolar-
120 DamID [19]. ESCs were grown on a thin polyester membrane that can be cut with a fine laser (**Fig. 1a,b**).
121 In brightfield microscopy, the nucleolus appears as a distinct, dark, and dense region within the nucleus,
122 allowing us to visualize and excise it using laser capture microdissection (LCM). The isolated nucleolus
123 was then collected into the cap of a microcentrifuge tube using MMI CapSure technology. The DNA
124 content of each nucleolus was purified and amplified via quasilinear whole-genome amplification (WGA)
125 [27]. To prevent any loss of DNA, WGA was carried out in the same tube in which the microdissected
126 nucleolus was collected. Before proceeding with library preparation and DNA sequencing, the purity of

127 nucleolar DNA was assessed by PCR to determine the presence of rRNA genes, which are located
128 within nucleoli, and the absence of *Tuba1*, an active gene that previous studies have shown to not
129 contact nucleoli[19] (**Extended Data Fig. 1a**).
130 We generated 53 high-quality single nucleolus contacts maps from ESCs, with a median of $5{\cdot}10^5$
131 uniquely mapped reads per nucleolus (**Fig. 1c, Extended Data Figs. 1b and 2**). We binned the genome
132 into 100 kb segments and called NADs using SICER2 [28] at a 100kb resolution using genomic DNA as
133 a control. The identified reads over the reference genome showed a bimodal distribution, indicating that
134 loci are either in a "contact" or "no contact" state with nucleoli (**Fig. 1c, Extended Data Fig. 1b**). Since
135 the microdissection of nucleoli will inevitably include genomic sequences above and below nucleoli, we
136 analysed the data by calculating the nucleolar contact frequency (CF) that we defined as the proportion
137 of microdissected nucleoli containing a defined NAD sequence (**Fig. 1d**). We found that NADs from
138 rDNA-chromosomes have higher CF than chromosomes not containing rRNA genes, underscoring the
139 specificity of NoLMseq in identifying NADs. Moreover, chromosome X, which is active in the analysed
140 male ESCs, showed the lowest nucleolar CF. For all downstream analyses, we selected NADs with
141 CF> 20%, a value that corresponds to FDR 0.0009. The analysis of NAD coverage/chromosome of all
142 53 nucleoli further supported the high propensity of rDNA-chromosomes to contact nucleoli relative to
143 the other chromosomes (**Fig. 1e**). Furthermore, the analysis of 53 microdissected nucleoli appears to
144 be sufficient for robust NAD identification. Calculation of nucleolar contact frequencies and genome
145 coverage using subsets of 20, 30, and 40 randomly selected nucleoli indicates that NAD saturation is
146 reached by 40 nucleoli (**Extended Data Fig. 1c,d**).
147 The average NAD coverage in single nucleoli was about 15%, much lower than the 30% NAD coverage
148 obtained from previous NAD studies in ESC population [17,19] (**Figs. 1e,f**). The data also showed that the
149 average length of NADs of rDNA-chromosomes was 1.85 Mb and significantly higher than the average
150 NAD size from the rest of the chromosomes (1.30 Mb, **Fig. 1g**). The accuracy of NoLMseq was also
151 supported by finding >90% NADs overlapping with previous NAD profiles from ESC populations using
152 Nucleolar-DamID [19] and SPRITE method [29] (**Fig. 1h**). To further validate the data, we used an
153 orthogonal approach by computing the CF of NADs from NoLMseq genomic data and their distance to
154 Fibrillarin marked nucleoli obtained by seqFISH+ microscopy [30] (**Fig. 1i**). We observed that nucleolar
155 CFs measured by NoLMseq were inversely proportional to the distance of NADs to the nucleolar marker
156 Fibrillarin, indicating that NoLMseq accurately measures genomic distance to nucleoli.

157 To further support the efficacy of NoLMseq, we analysed known NAD features of the identified NADs.
158 It is well known that centromeres tend to be positioned close to the nucleolus in various model systems.
159 Since in mouse cells all chromosomes are acrocentric, we measured the average NAD coverage at
160 centromere-proximal regions at the 5'-quintile portion of all chromosomes and found that it increases
161 with nucleolar CF, further supporting the accuracy of NoLMseq to identify sequences in contact with
162 nucleoli (**Fig. 2a**). Consistent with previous results in ESC populations obtained with Nucleolar-DamID
163 [19], NADs identified by NoLMseq were significantly depleted of active histone marks relative to
164 sequences within the active A compartment, showed a significant enrichment for the repressive
165 H3K9me2 but not for the other repressive marks H3K27me3 and H3K9me3, and displayed low gene
166 expression levels (**Fig. 2b,c**). Although NADs generally appear to have a repressive chromatin and
167 gene expression state, we could also find cases where highly expressed genes have high nucleolar
168 CFs. In particular, we found high nucleolar CFs for ribosomal protein (RP) genes, which encode proteins
169 for ribosome assembly in nucleoli and are transcribed by RNA Pol II, and tRNA genes, which are
170 transcribed by Pol III (**Fig. 2d**). In contrast, snoRNA genes, which express RNAs playing an important
171 role in rRNA modifications in nucleoli, did not show any preferential location to nucleoli. The nucleolar
172 contacts of RP and tRNA genes was not due to their location at rDNA-chromosomes since most of them
173 were located at chromosomes non containing rRNA genes (92% and 90%, respectively; **Extended**
174 **Data Fig. 3**). These results raise the possibility that nucleolus proximity could play a role in regulating
175 RP genes and ribosome biogenesis, as well as tRNA, potentially influencing protein translation on a
176 broader scale (**Fig. 5b**). Finally, these data also suggested that not all NADs are necessarily
177 transcriptionally repressed.
178 NADs have been previously characterized in two categories; NAD-only (or Type-1) which correspond
179 to sequences contacting nucleoli but not the nuclear lamina (NL) and NAD/LAD (or Type-2) which are
180 regions that can be located both at nucleoli and NL [13,17-19]. Since this classification of NADs was
181 obtained from ESC population, it has remained elusive whether NAD/LAD regions contact both the
182 nucleoli as well as the NL in the same or different cells. The analysis of single nucleoli data revealed
183 that NAD-only sequences have higher CF values than NAD/LAD, suggesting that NAD/LAD domains
184 can contact the nucleolus in one cell and the NL in another cell, but rarely both nucleolus and NL in the
185 same cell (**Fig. 2e**). We also observed an inverse correlation of NAD-only CF values and H3K27ac
186 content, indicating that strong NADs generally exhibit low levels of active chromatin (**Fig. 2f**). Similarly,

187 NAD-only domains with high nucleolar CF have high H3K9me2 levels (**Fig. 2g**). However, while
188 NAD/LAD regions showed significantly lower gene expression levels relative to genes within the active
189 A compartment, the expression of genes within NAD-only regions was not significantly reduced, albeit
190 there was a tendency to be low expressed when located at regions with the highest nucleolar CF (**Fig.**
191 **2h**). These results are consistent with the data described above showing that some active genes can
192 also contact nucleoli.
193
194 **ESCs are composed of two populations with distinct nucleolar contacts**
195 NADs obtained from single nucleoli allowed to study the degree of cell heterogeneity in genome
196 organization. We calculated the NAD coverage for each chromosome in single cells and performed
197 hierarchical clustering (**Fig. 3a**). We found two main ESC populations that differ according to the level
198 of nucleolar contacts among chromosomes. The major differences between these two groups were on
199 the level of rDNA-chromosome contacts with the nucleolus, which showed a mutually exclusive
200 relationship. rDNA-chromosomes 12 and 19 had high levels of nucleolar contacts in population 1
201 whereas they were almost absent in nucleoli of population 2 (**Fig. 3b**). In contrast, rDNA-chromosomes
202 16 and 18 displayed higher NAD coverage in population 2 than in population 1. In the case of
203 chromosomes not bearing rRNA genes, chromosomes 7, 11, 15, and 2 showed more nucleolar contacts
204 in population 2 than in population 1 whereas chromosomes 3 and 5 preferentially contact nucleoli of
205 population 1. Although ESCs are predominantly in the S phase, the potential influence of cell cycle
206 factors cannot be entirely ruled out. Nonetheless, it is notable that the analysis of histone modifications
207 revealed that NADs enriched in population 1 were significantly depleted of active histone marks and
208 enriched in H3K9me2 relative to NADs of population 2, suggesting different chromatin states between
209 these two ESC populations (**Fig. 3d**). Thus, the data revealed heterogeneity in the ESC genome
210 structure and chromatin configuration that depend on the genome organization around nucleoli.
211
212 **Detachment of NADs upon differentiation into NPCs results in gene activation**
213 Next, we asked whether the composition of genomic contacts in single nucleoli could change upon
214 differentiation of ESCs into neural progenitors (NPCs). As in the case of ESCs, in NPCs NADs from
215 rDNA- chromosomes consistently exhibited higher nucleolar CF than regions from other chromosomes
216 (**Fig. 4a**). However, NPCs displayed fewer NADs than ESCs, with a large proportion (75%) being the

217 same NADs as found in ESCs (**Fig. 4b-d**). Moreover, we observed more variability in nucleolus
218 association in ESCs than in NPCs as indicated by the Yule's Q coefficient, which provides a measure
219 of similarity between single-cell NADs (**Fig. 4e**). The NAD detection in single NPC nucleoli obtained
220 with NoLMseq is consistent with previous studies performed in NPC populations showing that the
221 architecture of chromosomes surrounding the nucleolus is in a more compact and rigid form whereas
222 in ESCs it appears more flexible and variable [19]. Moreover, these data are consistent with previous
223 reports indicating that ESCs harbour a more open and dynamic chromatin than differentiated cells [31,32].
224 Next, we investigated whether genes contacting nucleoli in ESCs but detaching from nucleoli in NPCs
225 (ESC specific NADs, ESC_{sp}-NADs) could change their expression state in NPCs. We defined ESC_{sp}-
226 NADs those NADs with nucleolar CF > 25% in ESCs and < 10% in NPCs. RNAseq data analysis
227 revealed that ESC_{sp}-NADs are less expressed in ESCs than in NPCs, suggesting that the detachment
228 from nucleoli facilitates gene activation (**Fig. 4f,g**). Moreover, the absoluted fold change in gene
229 expression in NPCs compared to ESCs was higher for the upregulated genes, with a large fraction
230 (60%) not expressed in ESCs (**Fig. 4h,i**). Accordingly, GO terms for these upregulated genes were
231 significantly linked to developmental processes, in particularly nervous system development, whereas
232 downregulated genes were mainly implicated in metabolic processes (**Extended Data Fig. 4**). These
233 results ishow that the detachment of genes from nucleoli during ESC differentiation unlocks them for
234 activation, indicating a regulatory role of the nucleolus for the establishment or maintenance of
235 repressive chromatin states.
236
237 **Nucleolar integrity is required for genomic contacts with nucleoli**
238 Nucleolus structure is highly dynamic and promptly responds to external stimuli that affect ribosome
239 biogenesis and nucleolar structure. For example, downregulation of rDNA transcription by treatment
240 with low doses of Actinomycin D (ActD) induces a spatial reorganization of the nucleolar structure,
241 including the migration of rRNA genes to the nucleolar periphery, forming the so-called nucleolar caps,
242 and the release of the granular component (GC) protein NPM1 from nucleoli (**Fig. 5a**) [33]. However, until
243 now, it could not be investigated whether these structural changes can impact the organization of the
244 genome around nucleoli mainly due to the technical limitations of the current technologies to map NADs
245 under conditions in which nucleolar integrity is affected. Since nucleoli in ESCs treated with ActD
246 (ESCs+ActD) are still detectable with brightfield microscopy, we reasoned that NoLMseq could be

247 applied to determine how nucleolus integrity affects chromosome contacts with nucleoli. Compared to
248 untreated cells, the average NAD coverage in ESC+ActD significantly decreased from 15% to 10%
249 (**Fig. 5b,c, Extended Data Fig. 5a**). Although NoLMseq revealed a substantial loss of nucleolar
250 contacts across all chromosomes, the majority of NADs retained upon ActD treatment were from the
251 rDNA-chromosomes (**Fig. 5d**). We validated this loss of contacts with nucleoli in ESCs+ActD by
252 quantitative DNA-FISH, using probes targeting four NADs at chromosomes 1, 2, 5, and 19 that were
253 previously identified and validated by Nucleolar-DamID [19] (**Fig. 5e,f, Extended Data Fig. 5b**). These
254 are strong NADs since they contact nucleoli in 70-95% of ESCs (**Fig. 5f**). The DNA-FISH probe for the
255 rDNA-chromosome 19 targeted a NAD sequence proximal to the rDNA locus. Accordingly, this NAD
256 remained anchored to nucleoli upon ActD treatment, an expected result since rRNA genes remain close
257 to nucleoli by forming nucleolar caps (**Fig. 5f**). In contrast, DNA-FISH probes targeting NADs at
258 chromosomes 1, 2, and 5 showed a significant detachment of NADs from the nucleoli upon ActD
259 treatment, indicating that nucleolar integrity is crucial for NAD association with nucleoli and supporting
260 the results obtained with NoLMseq. Because of the retainment of rDNA-chromosomes to nucleoli in
261 ESC+ActD, we reasoned that regions from rDNA-chromosomes still able to contact nucleoli in
262 ESC+ActD should correspond to centromere-proximal sequences, which are linearly located close to
263 rRNA genes. Accordingly, NAD coverage of centromere-proximal sequences of rDNA-chromosomes
264 was higher than the corresponding NAD coverage in untreated ESCs, suggesting a reorganization of
265 rDNA-chromosomes structure around nucleoli (**Fig. 5g**). In contrast, NAD coverage of centromere-
266 proximal sequences of chromosomes not bearing rDNA repeats showed a significant reduction
267 compared to NADs of untreated cells, further indicating that the anchoring of these sequences to
268 nucleoli depends on nucleoli integrity. All these results indicate that nucleolar integrity is an important
269 determinant for chromosome organization around nucleoli. To assess whether the detachment of NADs
270 from nucleoli upon nucleolar stress affects gene expression, we performed quantitative RNAseq spiked-
271 in with *ERCC* control RNAs (**Fig. 5h**). Treatment with ActD significantly altered the expression of 5382
272 genes ($\log_2$ fold change ≥ 1; $P < 0.05$), of which 2263 genes were upregulated and 3118 were
273 downregulated compared to control cells. Notably, 40% of the upregulated genes corresponded to those
274 detaching from the nucleoli, while only 23% of the downregulated genes were NAD genes that lost
275 contact with nucleoli upon ActD treatment (**Fig. 5i**). The upregulated NAD-genes were linked to
276 signaling pathways involving calcium, PI3K-Akt, and p53, the latter being well known to be activated by

277 RNA Pol I inhibition upon ActD treatment [34,35] (**Extended Data Fig. 5c**). These results indicate that the
278 detachment of genes from nucleoli, when nucleolar integrity is compromised, leads to their
279 transcriptional activation (**Fig. 5j**). Together with the reactivation of NAD genes during ESC
280 differentiation into NPCs upon loss of nucleolar contact, these results demonstrate an active role of the
281 nucleolus in repressing gene expression. Moreover, the data demonstrate that NoLMseq is a unique
282 and only genomic method for studying the role of nucleolus in genome organization under nucleolar
283 stress conditions that affect nucleolar integrity.
284
285 **Genomic contacts with nucleoli are predominantly mono-allelic**
286 Recent data have started to detect allelic asymmetry in gene expression and 3D-genome organization
287 [36,37]. So far, however, all studies on NADs were performed using cells whose maternal and paternal
288 chromosomes could not be distinguished from each other, as in the case of the E14 ESC line that
289 derives from a fully inbred homozygous mouse strain. Consequently, the information on NAD coverage
290 has been based on the assumption that both alleles contact nucleoli. To determine the allelic distribution
291 of NADs in single nucleoli, we applied NoLMseq to the male mouse F123-ESC line that was derived
292 from the F1 generation of two fully inbred homozygous mouse strains: *Mus musculus castaneus* (CAST,
293 paternal chromosomes) and *Mus musculus domesticus* S129S4/SvJae (S129, maternal chromosomes)
294 [38]. The F123 DNA sequence has been well characterized and contains high density of single nucleotide
295 variants (SNVs), with an average of 1 SNV every 124 nucleotides across autosomes [39]. We analysed
296 NAD profiles from 50 microdissected nucleoli of F123-ESCs by aligning them against the F123 genome
297 to identify allele-specific NADs (i.e., NAD_{S129} and NAD_{CAST}) (**Fig. 6a**). The vast majority (93%) of total
298 NADs identified in F123-ESCs corresponded to NADs identified in E14-ESCs, indicating that genomic
299 contacts with nucleoli are generally conserved between cell lines with the same developmental stage
300 but from different strains (**Extended Data Fig. 6a**). NADs of F123-ESCs showed a slightly lower
301 genome coverage (11.3%, calculated to haploid genome) relative to 15% NAD coverage measured in
302 E14-ESCs (**Fig. 6B**). Surprisingly, we found that a large fraction of NADs (86%) are mono-allelic (**Fig.
303 6a-c**). Monoallelic NADs were equally distributed among S129 and CAST chromosomes (**Extended
304 Data Fig. 6b**). The distinction between monoallelic and biallelic NADs was also evident from nucleolus
305 CF analysis, which showed that biallelic NADs have a higher CF than monoallelic NADs whereas NAD-
306 only and NAD/LAD regions display similar content (**Extended Data Fig. 6c**). We validated these results

307 by DNA-FISH for two strong NADs, one located at chromosome 5 and another located at the rDNA-
308 chromosome 19 and close to the rDNA locus (**Fig. 6d**). The NAD of chromosome 5 showed monoallelic
309 contacts in almost all the cells. Remarkably, even the NAD of chromosome 19 located close to the
310 rDNA locus showed mono-allelic contacts with nucleoli in 50% of the cells, supporting the results of
311 NoLMseq. This prevalent mono-allelic NAD distribution resulted in a much lower NAD coverage per cell
312 (5.6%, 297 Mbp) compared to the previously assumed bi-allelic distribution (**Fig. 6e**). To determine
313 whether mono- and bi-allelic NADs reflect differences in chromatin modifications, we performed
314 ChIPseq analysis for H3K9me2, H3K27ac, and H3K4me3 in F123-ESCs (**Fig. 6f**). We found that bi-
315 allelic NADs are in a more repressed chromatin states than mono-allelic NADs since they display
316 reduced levels of H3K27ac and H3K4me3 and higher levels of H3K9me2, the latter the repressive
317 histone mark characterizing NADs in ESCs [19]. Similarly, RNAseq analyses showed a significantly lower
318 expression of genes located at bi-allelic NADs (**Fig. 6g**). Among genes located at bi-allelic NADs, we
319 found cell type specific transcription factors, such as *Gata6* and *TAF4b*, as well as genes linked to
320 metabolic pathways and neuroactive ligand-receptor interactions (**Extended Data Fig. 6c**). These
321 results further indicate that high-frequency contact with nucleoli, even at the allelic levels, results in a
322 more repressive state.
323 Next, we asked whether the mono-allelic distribution of NADs might be parent specific. We applied
324 stringent criteria to assign parent specific NADs, considering, for example, that a specific NAD_{S129}
325 should have >25% nucleolar CF with the S129 genome and <10% nucleolar CF with the CAST genome
326 (**Fig. 6h**). However, very few NADs (1% on both alleles) showed a parent specific distribution. This
327 indicates that, generally, in one cell it is the paternal allele contacting nucleoli while in another cell it is
328 the maternal allele (**Fig. 6h**).
329
330 **Discussion**
331 We described NoLMseq, a method able to measure genome organization around nucleoli in single
332 cells. LCM has been widely used in various omics approaches for isolating single cells or specific tissue
333 regions[22-26]. NoLMseq has adapted this technology to study subcellular genomic compartments,
334 specifically the nucleolus, enabling precise examination of the genome architecture surrounding the
335 nucleolus in single cells.

336 Relative to previous NAD methods, NoLMseq not only detects NADs in single nucleoli but it can also
337 be applied to study genome organization around nucleoli under conditions of nucleolar stress, which
338 profoundly alter nucleolar structure [6-9] and that could not be examined with current methods, making
339 elusive how genome structure around nucleoli responds to nucleolar stress. The data revealed a
340 profound reorganization of the genome around "stressed" nucleoli, such an increase in nucleolar
341 contacts of centromere-proximal sequences of rDNA-chromosomes while the rest of the chromosomes
342 lose their contact. The genomic data obtained by NoLMseq are also consistent with recent image
343 analyses showing that perturbation of nucleolus structure upon downregulation of the RNA polymerase
344 I subunit RPA194 reduced centromere-nucleolus interactions [40]. These results indicate that nucleolar
345 structure and integrity plays an important role in genome organization and future studies will address
346 alterations in chromosomal interactions with nucleoli under pathological stress conditions impacting
347 ribosome biogenesis and how these perturbations are caused and their functional significance. The
348 results also showed that NADs are very dynamic and NoLMseq represents an unique technique able
349 to capture NADs at the present state rather than averages of the past and present states as in the case
350 of DamID as recently discussed [41].
351 The detection of NADs in single nucleoli using NoLMseq has proven to be highly precise compared to
352 previous methods and capable of providing unexplored insights in genome organization. For example,
353 NoLMseq determined that active genes, such as ribosomal protein genes and tRNA genes, also have
354 high frequency contacts with nucleoli. Interestingly, previous imaging analyses in living or fixed yeast
355 cells reported the proximity of some ribosomal protein genes and tRNA genes to nucleoli [42,43],
356 suggesting that the nucleolus could act as a compartment for the regulation of the expression of these
357 key components of the translation machinery. The presence of some active genes at nucleoli is also
358 consistent with a recent study showing that the localization of genes at the repressive B compartment
359 or proximal to nucleoli does not necessarily preclude transcription [44].
360 The accuracy of NoLMseq in detecting NADs relative to cell population studies is also shown by the
361 identification of ESC_{sp}-NADs that contain genes activated in NPCs, which could not be detected in
362 previous cell population studies [19]. Similarly, the results showing the activation of genes upon losing
363 contact with nucleoli upon ActD treatment indicate that the nucleolus serves an active role as a
364 repressive compartment. Because of the single nucleolus detection, NoLMseq revealed that ESCs
365 display a certain heterogeneity in genomic contacts, with nucleoli showing two major cell populations

366 with distinct chromatin features. Whether the presence of such populations, one more repressed than
367 the other one, might reflect differences in gene expression, pluripotency states, or other functions
368 remains to be investigated. These results are also consistent with recent data showing heterogeneity
369 of nuclear organization between individual single ESCs [45]. Finally, the application of NoLMseq in the
370 hybrid F123-ESC line showed that genomic contacts with nucleoli are mainly monoallelic. This result
371 clearly provided a more accurate value of NAD coverage, which was previously calculated based on
372 either a haploid genome or by assuming that all NADs are bi-allelic in the diploid genome. The average
373 NAD coverage 5.6% (i.e., ca. 297 Mbp) per cell obtained in the F123-ESC line is much lower than the
374 30% NAD coverage measured in ESC population studies using both purified nucleoli and Nucleolar-
375 DamID methods [17,19]. Although this calculated NAD coverage value does not include repetitive
376 sequences such as major and minor satellites, which are known to contact nucleoli but are not present
377 in the reference genome, it clearly represents a more realistic scenario than to have one third of
378 chromosomes contacting nucleoli. Moreover, the data showed that bi-allelic NADs have high nucleolar
379 CF are in a more repressive state than monoallelic NADs, further supporting the efficacy of NoLMseq
380 in identifying NADs and the nucleolus acting as a repressive compartment.
381 Together, the results demonstrate that NoLMseq not only accurately measures chromosome contacts
382 around single nucleoli but also provides novel insights into genome organization around nucleoli that
383 could not be detected by previous studies. We predict that NoLMseq will not only be a critical tool to
384 study genome organization around the nucleolus in biological populations but also to study how the 3D-
385 genome organization responds to nucleolar stress in disease states and understand the functional
386 consequence of these alterations.
387
388
389
390

391 **Materials and Methods:**

392 **Cell lines**

393 129 mouse embryonic stem cells (E14 line) were cultured in serum medium containing Dulbecco's
394 modified Eagle's medium + Glutamax (Life Technologies), 15% FCS (Life Technologies; Cat no.
395 10270106 FBS South American), 1× MEM NEAA (Life Technologies), 100 μM β-mercaptoethanol,
396 recombinant leukemia inhibitory factor, LIF (Polygene, 1000 U/ml), 1× penicillin/streptomycin (Life
397 Technologies). ESCs were seeded at a density of 50,000 cells/cm2 in culture dishes (Corning CellBIND
398 surface) coated with 0.1% gelatin without a feeder layer. Propagation of cells was carried out every 2
399 days using enzymatic cell dissociation. ESCs were treated with Actinomycin D (10ng/ml) for 24h before
400 downstream analyses.

401 Neural progenitor cells were generated from ESCs, according to a previously established protocol [46].
402 In brief, differentiation used a suspension-based embryoid bodies formation (Bacteriological Petri
403 Dishes, Bio-one with vents, Greiner). The neural differentiation media (DMEM, 10% fetal calf serum, 1×
404 MEM NEAA, 2 mM Pen/Strep, β-mercaptoethanol, and sodium pyruvate) was filtered through 0.22 μm
405 filters and stored at 4 °C. During the 8-day differentiation procedure, media was exchanged every 2
406 days. In the last 4 days of differentiation, the media was supplemented with 2 μM retinoic acid to
407 generate neural precursors that are Pax-6- positive radial glial cells.

408 F123-ESCs (mouse male, hybrid cell line, F1 S129/Jae and Cast mouse cross) [38] were cultured on a
409 layer of mitotically inactivated feeder murine embryonic fibroblasts under standard conditions (DMEM,
410 supplemented with 15 % KSR, 1x Glutamax, 10 mM non-essential amino acids, 50 μM beta-
411 mercaptoethanol, 1,000 U/ml LIF). Media was changed every 24h. Before harvesting, mESCs were
412 passaged onto feeder-free ESGRO-gelatin (EMD Millipore SF008). coated plates for at least 2
413 passages to remove feeder cells. Cells were harvested after approximately 48 h at 70 – 80 %
414 confluency. F123-ESCs were a gift from Bing Ren, University of California, San Diego.

415

416 **NoLMseq**

417 For laser-microdissection, cells were grown on ESGRO-gelatin coated and UV-irradiated PET
418 membrane slides (1.4um thick, RNase-free, MMI, 50102) for 24h. Cells were washed twice with 1X PBS
419 and fixed with EM-grade freshly-depolymerised 3% PFA in 1X PBS for 30mins. The slides were then
420 placed in 70% ethanol for 1min and air dried. The slides were then washed with filtered ultra-pure H_2O

421 (3x 1 min each) and air dried. Single nucleoli were laser microdissected with the MMI Laser Capture
422 Microdissection Nikon microscope (Molecular Machines & Industries) into single 0.2 ml tubes
423 (transparent MMI caps, 50208). Nucleoli were identified by bright-field imaging. A 0.2ml cap filled with
424 transparent adhesive material was lowered onto the cells. A laser was used to cut the PET membrane
425 surrounding each nucleolus and the cut PET membrane section along with the single nucleolus was
426 lifted off by the sticky cap. Each single nucleolus was collected in a separate cap and stored for further
427 processing. Identified nucleoli using bright-field microscopy were initially focused using Köhler
428 illumination to achieve optimal contrast for accurate visualization of the nucleoli. To ensure precision,
429 the stage was adjusted with camera-stage alignment, maintaining an inclination of less than ±0.1
430 degrees. Paraxial lens offset was employed to align the optical axes of all objectives. Laser alignment
431 was calibrated by firing a single shot, adjusting the pixel center of the imaging system to coincide with
432 the laser beam center. Laser cutting parameters, such as cut velocity, laser focus, and laser power,
433 were then optimized. The cut velocity was set at 20 μm/s, laser power at 0.001% of maximum capacity,
434 and the focus was calibrated for each cut to achieve a cut diameter of 0.25 μm thickness, ensuring
435 reproducibility. Prior to nucleolus excision, the laser was refocused on an empty area of the slide, where
436 a cut similar in size to the nucleolus was drawn. The laser's inner ring was positioned 0.25 μm from the
437 edge of the drawn shape. When the cap was lowered onto the membrane with the sample, any
438 membrane displacement (typically a few microns) was corrected using the Cap Z offset. To maintain
439 consistent focus during slide movement, slide surface focusing function of the microscope was
440 employed to account for potential topological differences in the membrane. Upon identifying a cell with
441 a distinct nucleolus, a 0.2 mL cap containing a transparent adhesive was lowered onto the sample. The
442 inner ring of the laser used to cut the PET membrane is positioned approximately 0.25 μm from the
443 outer edge of the nucleolus. The excised PET membrane, along with the nucleolus, was lifted off using
444 the adhesive cap. The cap was lowered onto an empty area of the membrane to check for the sample
445 was correctly excised. Any caps with improper cuts or those lacking a clearly identifiable nucleolus were
446 discarded. Only caps containing correctly isolated nucleoli were retained for further processing and
447 analysis. After collection, a new cap was added, and the entire focusing and cutting process was
448 repeated to ensure consistency across samples. Each nucleolus was collected in a separate cap for
449 further processing.

450 Whole-genome amplification (WGA) was carried out using the MALBAC single cell WGA kit (YK001A)
451 following manufacturer's recommendations with minor modifications. The entire WGA reaction was
452 carried out in the same 0.2ml tube with a single nucleolus. Another tube, with an empty section was
453 used as a negative control whereas 30 pg of whole cell DNA were used as a positive control for the
454 WGA reaction. The cell lysis reaction was first carried out by using a heated lid at 50 °C for 50 mins
455 and then samples were collected by briefly spinning and proceeding with the cell lysis reaction again at
456 50 °C for 50 mins, followed by inactivation at 80 °C for 10mins. The reaction is then cooled at 4 °C. The
457 lysis step is followed by a pre-amplification step which involves the quasilinear amplification using
458 random primers at 20 °C progressively with 10 °C steps till 70 °C. After cooling, the samples were
459 subjected to a final amplification step by 20 cycles of PCR.
460 WGA-amplified DNA was purified using a Qiagen MinElute PCR Purification Kit and eluted in 140 µl
461 ultrapure library-grade H_2O. The amplified nucleolar DNA was checked on a 2% agarose gel to select
462 positive samples showing smears corresponding to amplified DNA similar to the positive control. The
463 positive samples were further checked for the presence of rDNA and the absence of Tubulin gene by
464 PCR on an agarose gel. The samples which passed this quality control check were then used for library
465 preparation and sequencing. 120 µl of the reaction was first sonicated in split-cap tubes by Covaris
466 E220 to obtain fragments around 300-500nt in length (Peak power- 75, Duty factor- 20, cycle/bursts-
467 1000, duration- 35s). The samples were then purified and concentrated with AMPure XP beads
468 (Beckman Coulter, A63881) and used for Illumina library using the NEBNext ultra II kit (NEB E7600).
469 Briefly, NoLMseq samples (10-100 ng) were end-repaired and polyadenylated before the ligation of
470 Illumina compatible adapters. The adapters contain the index for multiplexing. Library concentrations
471 were estimated using a Qubit® 4 fluorometer (Thermo Fisher Scientific) and the 4200 TapeStation
472 system and libraries were pooled together in batches averaging 40 samples. Each library pool was
473 sequenced in single end 100bp in one lane of Novaseq6000 to get an average 10 million reads per
474 library.
475 For data analysis, NoLM-seq reads were aligned to the mouse mm10 reference genome using Bowtie2
476 (version 2.5.0; [47]) with default parameters. PCR duplicates were removed using samtools [48]. Positive
477 NAD bins were called using SICER2 [49], using the sequenced gDNA file as the control file and the
478 parameters w=100000, g=100000, fdr=0.0001. Bigwig files were created from the bam files using
479 bamCoverage from deeptools [50]. For F123-ESCs, N-masked genome was created using the mm10

480 reference genome and the Variant Call *Format* (VCF) file from the mouse genome project containing
481 the SNP information for all strains. The SNPsplit package [51] was used to read the VCF file and extract
482 the SNP information for the S129/SvJae and CAST strains and N-mask for the mm10 genome. The
483 reads were aligned using Bowtie2 to this N-masked reference genome using default parameters.
484 SNPsplit was then used to tag the SNPs for S129/SvJae and CAST alleles in the bam file and sort the
485 haplotype-specific bam files for both the alleles. bamCoverage and Sicer2 positive NAD calling was
486 performed independently on the allele-specific bam files. Integrative Genome Viewer (IGV, version
487 2.15.4) [52] was used to visualize and extract representative single nucleolus NoLMseq bigwig and bed
488 tracks.
489 Nucleolar contact frequency was calculated at a 100kb resolution. We defined as NADs sequences with
490 a > 20% nucleolar contact frequency that correspond to a false discovery rate (FDR) 0.0009 or 0.09%,
491 meaning that more than 99% of called NADs are truly NADs. This was calculated using the cumulative
492 distribution function (CDF) $\mathrm{P}(\mathrm{X} \leq \mathrm{k}) = \sum i = 0k(in)pi(1-p)n-1$ where "n" is the number of single
493 nucleoli samples, "p" is the probability that a false-positive region is present in the sample, "k" is the
494 contact frequency threshold. For the hierarchical clustering of NADs, NAD chromosome coverages in
495 single nucleoli were used for clustering single nucleoli based on divisive clustering (Diana) using the
496 "cluster" package (version 2.1.6) in R.
497
498 **RNAseq**
499 Total RNA was purified with TRIzol reagent (Life Technologies). The quality of the isolated RNA was
500 determined with a Qubit® 4 fluorometer (Life Technologies, California, USA) and 4200 TapeStation
501 system (Agilent, Santa Clara, California, USA). Only those samples with a 260 nm/280 nm ratio between
502 1.8–2.1 and a 28S/18S ratio within 1.5-2 were further processed. The TruSeq Stranded mRNA (Illumina,
503 Inc, California, USA) was used in the succeeding steps. Briefly, total RNA samples (100–1000 ng) were
504 polyA enriched and then reverse- transcribed into double-stranded cDNA. The cDNA samples were
505 fragmented, end-repaired and adenylated before ligation of TruSeq adapters containing unique dual
506 indices (UDI) for multiplexing. Fragments containing TruSeq adapters on both ends were selectively
507 enriched with PCR. The quality and quantity of the enriched libraries were validated using Qubit® 4
508 fluorometer. The product is a smear with an average fragment size of approximately 260 bp. Libraries
509 were normalized to 10 nM in Tris-Cl 10 mM, pH8.5 with 0.1% Tween 20. The NovaSeq X (Illumina, Inc,

510 California, USA) was used for cluster generation and sequencing according to standard protocol.
511 Sequencing was paired end at 2 × 150 bp.
512 The quality of the reads was checked by FastQC, a quality control tool for high throughput sequence
513 data [53]. The quality of the reads was increased by applying: a) SortMeRNA [54] (version 2.1) tool to filter
514 ribosomal RNA; b) Trimmomatic [55] (version 0.40) software package to trim the sorted (a) reads. N-
515 masked genome was created using the mm10 reference genome and the VCF file from the mouse
516 genome project containing the SNP information for all strains. The SNPsplit package [51] was used to
517 read in the VCF file and extract the SNP information for the S129/SvJae and CAST strains and N-mask
518 the mm10 genome. The sorted (a), trimmed (b) reads were mapped against the Nmasked mouse
519 genome (mm10) using the default parameters of the STAR (Spliced Transcripts Alignment to a
520 Reference, version 2.6, [56]). SNPsplit was then used to tag the SNPs for S129/SvJae and CAST alleles
521 in the bam file and sort the haplotype-specific bam files for both the alleles. For each gene, exon
522 coverage was calculated using a custom pipeline and then normalized in reads per kilobase per million
523 (RPKM) [57].
524 Cells were treated with Actinomycin D (10 ng/mL) for 24 hours, after which 1×10^6 cells were collected
525 for RNA purification using the Zymo RNA extraction kit (Zymo Research). Three biological replicates
526 were prepared for both ActD-treated and untreated conditions. RNA isolation was performed according
527 to the manufacturer's instructions. All samples were then spiked-in with ERCC control RNAs (Thermo
528 Fisher Scientific), following the manufacturer's recommendations.
529 Library preparation was carried out using the TruSeq Stranded mRNA kit (Illumina, Inc., California,
530 USA) as described previously. The absolute abundance of mRNA transcripts was assessed using the
531 ERCC92 RNA spike-in control[58]. Most of the 92 ERCC transcripts showed consistent counts between
532 untreated and ActD-treated samples. Reads were aligned to the mouse genome using STAR and a
533 custom pipeline was used to calculate RPKM values.
534
535 **ChIPseq**
536 ChIP analysis was performed as previously described [59]. Briefly, 1% formaldehyde was added to
537 cultured cells to cross-link proteins to DNA. Isolated nuclei were then lysed with lysis buffer (50 mM
538 Tris-HCl, pH 8.1, 10 mM EDTA, pH 8, 1% SDS, 1X protease inhibitor complete EDTA-free cocktail,
539 Roche). Nuclei were sonicated using a Bioruptor ultrasonic cell disruptor (Diagenode) to shear genomic

540 DNA to an average fragment size of 200 bp. 20 µg of chromatin was diluted to a total volume of 500 µl
541 with ChIP buffer (16.7 mM Tris-HCl, pH 8.1, 167 mM NaCl, 1.2 mM EDTA, 0.01% SDS, 1.1% Triton X-
542 100) and incubated overnight with the ChIP-grade antibodies against H3K9me2, H3K9me3,
543 H3K27me3, H3K4me1, H3K4me3 and H3K27ac. After washing, bound chromatin was eluted with the
544 elution buffer (1% SDS, 100 mM $NaHCO_3$). Upon proteinase K digestion (50 °C for 3 h) and reversion
545 of cross- linking (65 °C, overnight), DNA was purified with phenol/chloroform, and ethanol precipitated.
546 The quality and quantity of the isolated DNA were determined with a Qubit® 4 Fluorometer (Life
547 Technologies, California, USA) and the 4200 TapeStation system. Briefly, ChIP samples (1 ng) were
548 end-repaired and polyadenylated before the ligation of Illumina compatible adapters. The adapters
549 contain the index for multiplexing. The quality and quantity of the enriched libraries were validated using
550 Qubit® 4 Fluorometer and the 4200 TapeStation system. The libraries were pooled to 10 nM in Tris-Cl
551 10 mM, pH8.5 with 0.1% Tween 20. Sequencing was performed on the NovaSeq 6000 for 100bp single
552 end reads (Illumina, Inc, California, USA).
553 For F123-ESCs, N-masked genome was created using the mm10 reference genome and the Variant
554 Call Format (VCF) file from the mouse genome project containing the SNP information for all strains.
555 The SNPsplit package [51] was used to read the VCF file and extract the SNP information for the
556 S129/SvJae and CAST strains and N-mask for the mm10 genome. ChIPseq reads were aligned to the
557 N-masked mm10 reference genome with Bowtie2 (version 2.5.0; (version 2.5.0; [47]) using default
558 parameters. PCR duplicates were removed using samtools [48]. SNPsplit was then used to tag the SNPs
559 for S129/SvJae and CAST alleles in the bam file and sort the haplotype-specific bam files for both the
560 alleles. Bigwig files were created from the bam files using bamCoverage from deeptools [50] using default
561 parameters. Integrative Genome Viewer (IGV, version 2.15.4) [52] was used to visualize and extract
562 representative ChIPseq tracks.
563
564 **Gene Ontology (GO) enrichment:**
565 GO enrichment analysis of genes was performed with DAVID 6.8 [60]. All genes in *Mus musculus* were
566 used as the background.
567
568
569

570 **DNA-FISH**

571 DNA-FISH probes for chromosomes 1, 2, 5, and 19 were generated as previously described [19]. The
572 probes were obtained with oligopaint libraries that were constructed the PaintSHOP interface created
573 by the Beliveau lab and were ordered from CustomArray/Genscript in the 12 K Oligopool format. Each
574 library contains a universal primer pair used to amplify all the probes in the library, followed by a specific
575 primer pair hooked to the 40-46-mer genomic sequences, for a total probe of around 124-130-mers.
576 Oligopaint libraries were produced by emulsion PCR from the pool, followed by a "two-step PCR" and
577 lambda exonuclease as described before [19,61]. Specifically, the emulsion PCR with the universal primers
578 allowed amplifying all pool of probes in the library. The "two-step PCR" led to the addition of a tail to the
579 specific probes bound to the Alexa Fluor 488 fluorochrome. All oligonucleotides were purchased from
580 Integrated DNA Technologies (IDT, Leuven, Belgium).

581 DNA-FISH was adapted from the protocol of Cavalli's lab [62]. Cells fixed with 4% PFA for 10 min at room
582 temperature 24h after seeding. Cells were washed three times with 1X PBS and then permeabilized
583 with 0.5%Triton-X100/PBS for 10 min on ice, followed by 10 min at room temperature. After three
584 additional washes with 1X PBS, cells were incubated with 0.1 M HCl for 10 min at room temperature,
585 washed twice with 2X SCCT, and twice with 50% Formamide-2X SCCT for 20min, firstly at room
586 temperature and then at 60°C. Probe mixture contained around 45pmol of Oligopaint probe, 0,8µL of
587 ribonuclease A (ThermoScientific, 10 mg/mL), and FISH hybridization buffer for a total mixture volume
588 of 20uL, which was directly added on the slide. Cell DNA was denaturated at 83 °C for 8 min, and
589 hybridization was performed in a humid dark chamber overnight at 42 °C. Cells were washed with 2X
590 SCCT for 15 min once at 60°C and once at room temepature, once with 0.2X SCC for 10 min, twice
591 with 1X PBS for 2 min, and three times with 1X PBT for 2 min. Slides were then incubated for 1 h at
592 room temperature with blocking solution in a dark humid chamber, and overnight at 4 °C with primary
593 antibody against Nucleolin. Cells were washed four times with 1X PBT at increasing incubation times
594 (1 × 2 min, 1 × 3 min, 2 × 5 min) and then incubated for 2 h at room temperature with goat anti-mouse
595 IgG (H + L) Alexa Fluor 546 in a dark humid chamber. Slides were washed four times with 1X PBT at
596 increasing incubation times (1 × 2 min, 1 × 3 min, 2 × 5 min), three times with 1X PBS for 2 min. Then,
597 slides were mounted with Vectashield DAPI mounting media (Vector, H-1200) and, after drying, stored
598 at 4 °C.

599 DNA FISH/IF samples were imaged using a Zeiss LSM 980 Airyscan, with a z-stack collected for each
600 channel (step size, 0.3 um), using the oil objective Plan-Apochromat/1.40. Images were processed by
601 ImageJ (version 2.14.0/1.54F). The individual cells were identified by Hoechst/DAPI staining and cells
602 containing signal for DNA-FISH channel were identified manually on the corresponding fluorescent
603 channel. Distance between the DNA-FISH signal and the nucleolar marker immunofluorescence signal
604 was calculated using ImageJ (version 2.14.0/1.54F) and used to count the number of foci contacting
605 nucleolus and the number of cells with at least one contact with the nucleolus.
606
607 **Published datasets**
608 Published datasets used in the study were from: H3K27ac-, H3K4me1-, H3K27me3-ChIP-seq [46]
609 (GSE72164); H3K4me3- and H3K9me3-ChIPseq [63] (GSE23943); H3K9me2-ChIPseq [64] (GSE77420);
610 A/B compartments [65]; Nucleolar DamID and RNAseq in ESCs and NPCs [19] (GSE150822); Lamin-
611 DamID [66] (GSE17051); SPRITE [29] (GSE114242); seqFISH+ [30].
612
613 **Acknowledgements**
614 This work was supported by the ERC grant (ERC-AdG-787074-NucleolusChromatin), Swiss National
615 Science Foundation (31003B-201268; 320030-227818), and EMBO Postdoctoral Fellowship (ALTF
616 209-2021) and the Forschungskredit of the University of Zurich to K.W. We thank Catherine Aquino and
617 the Functional Genomic Center Zurich for the assistance in sequenscing. We thank the Scientific Center
618 for Optical and Electron Microscopy of ETH Zurich for support and assistance in LCM. We thank Ana
619 Pombo for her technical advises on laser-microdissection and library preparation and Bing Ren for the
620 F123-ESC line.
621
622 **Author contributions**
623 K.W. and J.K-R. established the NoLMseq. K.W. performed NoLMseq in all the described conditions,
624 ChIPseq and RNAseq in F123-ESCs and all data analyses of NADs. S.G. and M.R. performed DNA-
625 FISH analyses. C.M. performed IF analyses. K.W. and R.S. wrote the manuscript. R.S conceived and
626 supervised the project.
627
628

629 **Declaration of interests**

630 The authors declare no competing interests.

631

632 **Figure legends**

633 **Figure 1**

634 **NoLMseq identifies NADs in single cells**

635 **a.** Scheme representing the nucleolar laser capture microdissection (NoLMseq).

636 **b.** Representative images of ESCs before and after nucleolar laser capture microdissection.

637 **c.** Nucleolar contacts maps from 53 single nucleoli for chromosomes 6, 8, and 19. Black bars indicates

638 NADs.

639 **d.** Cumulative histogram of genome-wide nucleolar contact frequency (CF) values with respect to their

640 location at chromosomes containing rRNA genes (rDNA-chromosomes), without (w/o rDNA), and X and

641 Y chromosomes.

642 **e.** Coverage of NADs with CF > 20% on each chromosome in single nucleoli. Dotted grey line indicates

643 the mean NAD coverage in single cells. Black lines indicate the mean on each chromosome.

644 **f.** Violin plot showing NAD coverage in single cells. Red dashed line indicates the median.

645 **g.** Size of NADs located at rDNA-chromosomes and chromosomes not bearing rRNA genes (w/o rDNA).

646 Red and blue lines indicate medians, and the dotted lines indicate quartiles. Statistical significance (*P*-

647 values) was calculated using unpaired t-test (**** < 0.0001).

648 **h.** Coverage of NADs identified by NoLMseq relative to NADs identified in ESC populations with the

649 Nucleolar-DamID [19] and SPRITE [29] method.

650 **i.** Genome-wide comparison of DNA seqFISH+ distance to exterior of nucleoli marked with Fibrillarin

651 (µm) [30] and NoLMseq NAD contact frequency for 3713 paired genomic regions. Tukey boxplot where

652 box limits represent the 25th and 75th percentiles and the black line represents the median. Statistical

653 significance (*P*-values) was calculated using unpaired t-test (** < 0.01; **** < 0.0001).

654

655 **Figure 2**

656 **NADs identified by NoLMseq correspond to repressive chromatin domains**

657 **a.** NAD coverage on the centromere-proximal regions (5' -quintile) as a function of nucleolar contact

658 frequency.

659 **b.** Levels of active histone marks (H3K27ac, H3K4me1, H3K4me3) and repressive histone marks

660 (H3K9me2, H3K9me3, H3K27me3) at NADs relative to genomic regions located at the active A

661 compartment (A comp.). Values are shown as average RPKM. Tukey boxplot where box limits represent

662 the 25th and 75th percentiles. The horizontal line within the boxes represents the median. Statistical
663 significance (*P*-values) was calculated using the unpaired two-tailed t test (**<0.01, ****<0.0001, ns:
664 nonsignificant).
665 **c.** Expression values (RPKM) of genes within the active A compartment (A Comp.) and NADs. Tukey
666 boxplot where box limits represent the 25th and 75th percentiles. The horizontal line within the boxes
667 represents the median. Statistical significance (*P*-values) was calculated using the unpaired two-tailed
668 t test(****<0.0001).
669 **d.** Gene densities of ribosomal protein genes (red), tRNA genes (black), snoRNA genes (pink) and all
670 genes (grey) as a function of nuclear CF.
671 **e.** Left panel shows nucleolar contact frequency for NAD-only and NAD/LAD sequences. Right panel
672 depicts how NAD-only and NAD/LAD contact nucleoli in single cells.
673 **f,g,h.** Levels of H3K27ac (**f**), H3K9me2 (**g**), and gene expression (**h**) at NAD-only and NAD/LAD as a
674 function of nucleolar CF relative to the active A compartment (A comp.). at the active A compartment
675 (A Comp.) and at NAD-only and NAD/LAD relative to nucleolar CF. Values are shown as average
676 RPKM. Tukey boxplot where box limits represent the 25th and 75th percentiles. The horizontal line
677 within the boxes represents the median. Statistical significance (*P*-values) was calculated using the
678 unpaired two-tailed t test (**<0.01, ***< 0.001, ****<0.0001, ns: nonsignificant).
679
680 **Figure 3**
681 **ESCs showed two populations with distinct nucleolar contacts**
682 **a.** Hierarchical clustering of nucleoli according to their NAD coverage/chromosome
683 **b.** NAD coverage at the indicated chromosomes in the top quartile NADs of the two ESC populations.
684 **c.** Scheme representing the contact with nucleoli of the rDNA-chromosomes with the nucleoli in the two
685 ESC populations.
686 **d.** Levels of active histone marks (H3K4me1, H3K4me3, H3K27ac) and repressive histone marks
687 (H3K9me2, H3K9me3, H3K27me3) at NADs enriched in ESC population (Pop) 1 or 2. Values are shown
688 as average RPKM. Tukey boxplot where box limits represent the 25th and 75th percentiles. The
689 horizontal line within the boxes represents the median. Statistical significance (*P*-values) was calculated
690 using the unpaired two-tailed t test (*<0.05, ****<0.0001, ns: nonsignificant).
691

692 **Figure 4**

693 **NADs from single nucleoli of neural progenitors**

694 **a.** Cumulative histogram of genome-wide of nucleolar contact frequency measured from 23
695 microdissected nucleoli with respect to their location at chromosomes containing rRNA genes (rDNA-
696 chromosomes), without (w/o rDNA), and X and Y chromosomes in NPCs.

697 **b.** Coverage of NADs with CF > 20% on each chromosome in single nucleoli of NPCs. Dotted grey line
698 indicates the average NAD coverage in single cells of NPCs. Black lines indicate the mean on each
699 chromosome.

700 **c.** Violin plots showing NAD coverage in single ESCs and NPCs. Data from ESCs were also shown in
701 **Figure 1f**. Red dashed lines indicate the median and black dotted lines indicate the quartiles.

702 **d.** Venn diagram showing the distribution of NADs in ESCs and NPCs.

703 **e.** Violin plots showing the distribution of Yule's Q values as a measure of NAD cell-cell similarity in
704 ESCs and NPCs. Red dashed lines indicate the median and black dotted lines indicate the quartiles.

705 **f.** Expression levels of genes located at ESC_{sp}-NADs in ESCs and NPCs. Tukey boxplot where box
706 limits represent the 25th and 75th percentiles. The horizontal line within the boxes represents the
707 median. Statistical significance (*P*-values) was calculated using the paired two-tailed t test
708 (****<0.0001).

709 **g.** Scatter plot showing the expression levels of genes at ESC_{sp}-NADs in ESCs and NPCs. Expression
710 of genes significantly (P < 0.05) upregulated (blue) and downregulated (red) are shown.

711 **h.** Plot showing the absolute log_2 fold changes of upregulated and downregulated genes at ESC_{sp}-
712 NADs in NPCs. Black lines indicate the median. Statistical significance (*P*-values) was calculated using
713 the unpaired two-tailed t test (****<0.0001).

714 **i.** Proportion of low expressing genes (< 0.1 RPKM) in ESCs that are located at ESC_{sp}-NADs and are
715 up- or downregulated in NPCs.

716

717 **Figure 5**

718 **Nucleolar integrity is required for genomic contacts with nucleoli**

719 **a.** Left panel represents alterations in nucleolus structure upon treatment with Actinomycin D (ActD),
720 showing the re-organization of rRNA genes, which form nucleolar caps. Right panel shows
721 immunofluorescence images of the nucleolar markers UBF and NPM1. Scale bar is 9 μm.

722 **b.** Histogram showing the average NAD coverage/chromosome from single nucleoli of untreated ESCs
723 (blue) and 34 microdissected nucleoli from ESCs treated with ActD (grey).
724 **c.** Violin plots showing NAD coverage in single untreated ESCs (blue) and ESCs treated with ActD
725 (grey). Data from ESCs were also shown in **Figure 1F**. Red dashed lines indicate the median and black
726 dotted lines indicate the quartiles. Statistical significance (P-value) was calculated using the unpaired
727 two-tailed t test (****<0.0001).
728 **d.** Distribution of NADs in ESCs treated with ActD as a function of nucleolar CF across rDNA-
729 chromosomes, chromosomes without (w/o) rDNA, and NADs lost relative to untreated ESCs.
730 **e.** Representative immuno-FISH images for NAD at chromosome 2. Nucleolin serves as nucleolar
731 marker. Scale bar is 5 μm.
732 **f.** Box plots represent the quantifications of immuno-DNA-FISH analyses showing the percentage of
733 cells displaying NADs contacting nucleoli. Error bars represent s.d. Statistical significance (*P*-values)
734 from three independent experiments was calculated using Mann-Whitney test (** < 0.01; *** < 0.001;
735 ns: non-significant).
736 **g.** NAD coverage at the centromere-proximal regions (the first 5'-quintile) between rDNA-chromosomes
737 and chromosomes without (w/o) rDNA. rDNA on untreated ESCs and ESCs treated with ActD. Red
738 dashed lines indicate the median and black dotted lines indicate the quartiles. Statistical significance
739 (P-value) was calculated using the unpaired two-tailed t test (**<0.01).
740 **h.** Volcano plot showing fold change (log_2 values) in transcript levels of ESC+ActD and control ESCs.
741 Gene expression values of three replicates were averaged and selected for log2 fold changes ≥ 1and
742 adjusted (adj.) $P < 0.05$. Upregulated and downregulated genes at detached NADs are shown.
743 **i.** Pie chart showing the proportion of upregulated and downregulated NAD-genes detached from
744 nucleoli in ESC+ActD relative to all significantly regulated genes (log2 fold changes ≥ 1 and adj. $P <$
745 0.05.
746 **j.** Schematic representation of alterations in genomic contacts with nucleoli and gene expression
747 following ActD treatment. The upregulation of genes detaching from nucleoli, the formation of nucleolar
748 caps, and the increased frequency of centromere-proximal contacts with rDNA chromosomes are
749 shown.
750
751 **Figure 6**

752 **Genomic contacts with nucleoli are mono-allelic**

753 **a.** NoLMseq tracks displaying NAD sequences from four microdissected single nucleoli from hybrid
754 F123-ESCs (S129/CAST) on the total mm10 genome (black), maternal S129 genome (pink) and
755 paternal CAST genome (blue). Bars below the tracks indicate NADs called on respective genomes.

756 **b.** NAD coverage from single nucleoli calculated over the haploid genome. Median and quartiles are
757 shown. Statistical significance (P-value) was calculated using the unpaired two-tailed t test
758 (****<0.0001, ns: non-significant).

759 **c.** Proportion of bi-allelic and mono-allelic NADs in single nucleoli. Black dashed lines indicate median
760 and black dotted lines indicate quartiles. Statistical significance (P-value) was calculated using the
761 unpaired two-tailed t test (****<0.0001).

762 **d.** Left panel shows DNA-FISH images of a NAD located at chromosome 19. Right panel is the
763 quantification of bi-allelic and mono-allelic contacts with nucleoli. Scale bar is 5 μm. Error bars indicate
764 s.d.

765 **e.** NAD coverage from single nucleoli over the diploid genome. Black dashed line indicates the median
766 and black dotted lines indicate the quartiles.

767 **f,g.** Levels of H3K9me2, H3K27ac, and H3K4me3 (**F**) and gene expression (**G**) at bi-allelic and mono-
768 allelic NADs. Values are shown as average RPKM. Violin plots where black dashed lines indicate the
769 median and black dotted lines indicate the quartiles. Statistical significance (*P*-values) was calculated
770 using the unpaired two-tailed t test (**<0.01; ***<0.001; ****<0.0001).

771 **h.** Pie chart showing the amounts of paternal (NAD_{CAST}) and maternal (NAD_{S129}) NADs.

772 **i.** Model showing that mono-allelic distribution of NADs at nucleoli of single cells is generally not parent
773 specific.

774

775 **Extended Data figure legends**

776 **Extended Data Figure 1**

777 **NoLMseq identifies NADs in single cells**

778 **a.** Gel electrophoresis showing whole-genome amplification (WGA) of isolated nucleoli (left panel) and
779 the PCR amplification for rRNA genes and *Tuba1* sequences.

780 **b.** NoLMseq tracks from 6 microdissected nucleoli at chromosomes 6, 8, at 19. Black bars below the
781 tracks indicate NADs called in respective single nucleoli.

782 **c.** Cumulative histogram of genome-wide nucleolar contact frequency (CF) values in 20, 30, 40
783 randomly selected microdissected nucleoli and all the 53 analysed nucleoli. The location at
784 chromosomes containing rRNA genes (rDNA-chromosomes), without (non-rDNA chromosomes), and
785 X and Y chromosomes is shown.

786 **d.** NAD coverage calculated from 20, 30, 40 randomly selected microdissected nucleoli and all the 53
787 analysed nucleoli.

788

789 **Extended Data Figure 2**

790 **NAD contact frequency for each chromosome**

791 Nucleolus contact frequency for the 53 ESC nucleoli along the length of each chromosome. rDNA-
792 chromosomes are depicted with an orange line.

793

794 **Extended Data Figure 3**

795 **Ribosomal protein and tRNA genes show high nucleolar contact frequency**

796 Distribution of ribosomal protein and tRNA genes at rDNA-chromosomes and chromosomes not
797 containing rRNA genes (other chromosomes).

798

799 **Extended Data Figure 4**

800 **NADs from single nucleoli of neural progenitors**

801 Gene ontology (GO) terms for upregulated and downregulated genes at ESC_{sp}-NADs in NPCs.

802

803 **Extended Data Figure 5**

804 **Nucleolar integrity is required for genomic contacts with nucleoli**

805 **a.** Coverage of NADs at each chromosome of single nucleoli from ESCs treated without and with
806 Actinomycin D (ActD). Dotted grey line indicates the average NAD coverage in single cells. Black lines
807 indicate the mean on each chromosome.
808 **b.** Representation of the DNA-FISH probes targeting NADs at chromosomes 1, 2, 5, and 19, the latter
809 containing rRNA genes at the 5' end, close to the centromeric region. The corresponding NADs profiles
810 from Nucleolar-DamID [19] are shown. iNAD: genomic domains not interacting with nucleoli.
811 **c.** KEGG pathways for upregulated and downregulated NAD-genes detached from nucleoli in
812 ESC+ActD.
813
814 **Extended Data Figure 6**
815 **Genomic contacts with nucleoli are mono-allelic, but not parent specific.**
816 **a.** Pie chart showing the proportion of NADs identified in F123-ESCs that have also been found in E14-
817 ESCs.
818 **b.** Mono-allelic distribution of 129 and CAST genome around nucleoli of single cells. Black dashed lines
819 indicate median and black dotted lines indicate quartiles. Statistical significance (P-value) was
820 calculated using the unpaired two-tailed t test (ns: non-significant).
821 **c.** Cumulative histogram of nucleolar contact frequency (CF) values with respect to their mono-and
822 biallelic content for all NADs, NAD-only, and NAD/LAD.
823 **d.** Gene ontology (GO) terms of genes located on bi-allelic NADs.
824
825

826 **References**

827 1 Willemin, A., Szabo, D. & Pombo, A. Epigenetic regulatory layers in the 3D nucleus. *Mol Cell* **84**, 415-428
828 (2024). https://doi.org:10.1016/j.molcel.2023.12.032

829 2 Misteli, T. The Self-Organizing Genome: Principles of Genome Architecture and Function. *Cell* **183**, 28-45
830 (2020). https://doi.org:10.1016/j.cell.2020.09.014

831 3 Bersaglieri, C. & Santoro, R. Genome Organization in and around the Nucleolus. *Cells* **8(6)**, 579 (2019).
832 https://doi.org:10.3390/cells8060579

833 4 Bassler, J. & Hurt, E. Eukaryotic Ribosome Assembly. *Annu Rev Biochem* **88**, 281-306 (2019).
834 https://doi.org:10.1146/annurev-biochem-013118-110817

835 5 Pelletier, J., Thomas, G. & Volarevic, S. Ribosome biogenesis in cancer: new players and therapeutic avenues.
836 *Nat Rev Cancer* **18**, 51-63 (2018). https://doi.org:10.1038/nrc.2017.104

837 6 Derenzini, M. *et al.* Nucleolar size indicates the rapidity of cell proliferation in cancer tissues. *The Journal of*
838 *pathology* **191**, 181-186 (2000). https://doi.org:10.1002/(SICI)1096-9896(200006)191:2<181::AID-
839 PATH607>3.0.CO;2-V

840 7 Boisvert, F. M., van Koningsbruggen, S., Navascues, J. & Lamond, A. I. The multifunctional nucleolus. *Nat Rev*
841 *Mol Cell Biol* **8**, 574-585 (2007). https://doi.org:nrm2184 [pii] 10.1038/nrm2184

842 8 Goodfellow, S. J. & Zomerdijk, J. C. Basic mechanisms in RNA polymerase I transcription of the ribosomal RNA
843 genes. *Subcell Biochem* **61**, 211-236 (2013). https://doi.org:10.1007/978-94-007-4525-4_10

844 9 Ruggero, D. Revisiting the nucleolus: from marker to dynamic integrator of cancer signaling. *Sci Signal* **5**, pe38
845 (2012). https://doi.org:10.1126/scisignal.2003477

846 10 Corman, A., Sirozh, O., Lafarga, V. & Fernandez-Capetillo, O. Targeting the nucleolus as a therapeutic strategy
847 in human disease. *Trends Biochem Sci* **48**, 274-287 (2023). https://doi.org:10.1016/j.tibs.2022.09.006

848 11 Yang, K., Yang, J. & Yi, J. Nucleolar Stress: hallmarks, sensing mechanism and diseases. *Cell Stress* **2**, 125-
849 140 (2018). https://doi.org:10.15698/cst2018.06.139

850 12 Boukoura, S. & Larsen, D. H. Nucleolar organization and ribosomal DNA stability in response to DNA damage.
851 *Curr Opin Cell Biol* **89**, 102380 (2024). https://doi.org:10.1016/j.ceb.2024.102380

852 13 Bersaglieri, C. & Santoro, R. Methods for mapping 3D-chromosome architecture around nucleoli. *Curr Opin*
853 *Cell Biol* **81**, 102171 (2023). https://doi.org:10.1016/j.ceb.2023.102171

854 14 Kumar, P. *et al.* Nucleolus and centromere Tyramide Signal Amplification-Seq reveals variable localization of
855 heterochromatin in different cell types. *Commun Biol* **7**, 1135 (2024). https://doi.org:10.1038/s42003-024-
856 06838-7

857 15 Nemeth, A. *et al.* Initial genomics of the human nucleolus. *PLoS Genet* **6**, e1000889 (2010).
858 https://doi.org:10.1371/journal.pgen.1000889

859 16 Koningsbruggen, S. v. *et al.* High-Resolution Whole-Genome Sequencing Reveals That Specific Chromatin
860 Domains from Most Human Chromosomes Associate with Nucleoli. *Molecular Biology of the Cell* **21**, 3735-
861 3748 (2010). https://doi.org:10.1091/mbc.e10-06-0508

862 17 Bizhanova, A., Yan, A., Yu, J., Zhu, L. J. & Kaufman, P. D. Distinct features of nucleolus-associated domains
863 in mouse embryonic stem cells. *Chromosoma* (2020). https://doi.org:10.1007/s00412-020-00734-9

864 18 Vertii, A. *et al.* Two contrasting classes of nucleolus-associated domains in mouse fibroblast heterochromatin.
865 *Genome Res* **29**, 1235-1249 (2019). https://doi.org:10.1101/gr.247072.118

866 19 Bersaglieri, C. *et al.* Genome-wide maps of nucleolus interactions reveal distinct layers of repressive chromatin
867 domains. *Nat Commun* **13**, 1483 (2022). https://doi.org:10.1038/s41467-022-29146-2

868 20 Shore, D. & Albert, B. Ribosome biogenesis and the cellular energy economy. *Curr Biol* **32**, R611-R617 (2022).
869 https://doi.org:10.1016/j.cub.2022.04.083

870 21 Lempiainen, H. & Shore, D. Growth control and ribosome biogenesis. *Curr Opin Cell Biol* **21**, 855-863 (2009).
871 https://doi.org:10.1016/j.ceb.2009.09.002

872 22 Datta, S. *et al.* Laser capture microdissection: Big data from small samples. *Histol Histopathol* **30**, 1255-1269
873 (2015). https://doi.org:10.14670/HH-11-622

874 23 Beagrie, R. A. *et al.* Complex multi-enhancer contacts captured by genome architecture mapping. *Nature* **543**,
875 519-524 (2017). https://doi.org:10.1038/nature21411

876 24 Casasent, A. K. *et al.* Multiclonal Invasion in Breast Tumors Identified by Topographic Single Cell Sequencing.
877 *Cell* **172**, 205-217 e212 (2018). https://doi.org:10.1016/j.cell.2017.12.007

878 25 Nichterwitz, S., Benitez, J. A., Hoogstraaten, R., Deng, Q. & Hedlund, E. LCM-Seq: A Method for Spatial
879 Transcriptomic Profiling Using Laser Capture Microdissection Coupled with PolyA-Based RNA Sequencing.
880 *Methods Mol Biol* **1649**, 95-110 (2018). https://doi.org:10.1007/978-1-4939-7213-5_6

881 26 Chen, J. *et al.* Spatial transcriptomic analysis of cryosectioned tissue samples with Geo-seq. *Nat Protoc* **12**,
882 566-580 (2017). https://doi.org:10.1038/nprot.2017.003

883 27 Baslan, T. *et al.* Genome-wide copy number analysis of single cells. *Nat Protoc* **7**, 1024-1041 (2012).
884 https://doi.org:10.1038/nprot.2012.039

885 28 Zang, C. *et al.* A clustering approach for identification of enriched domains from histone modification ChIP-Seq
886 data. *Bioinformatics* **25**, 1952-1958 (2009). https://doi.org:10.1093/bioinformatics/btp340

887 29 Quinodoz, S. A. *et al.* Higher-Order Inter-chromosomal Hubs Shape 3D Genome Organization in the Nucleus.
888 *Cell* **174**, 744-757 e724 (2018). https://doi.org:10.1016/j.cell.2018.05.024

889 30 Takei, Y. *et al.* Integrated spatial genomics reveals global architecture of single nuclei. *Nature* **590**, 344-350
890 (2021). https://doi.org:10.1038/s41586-020-03126-2

891 31 Meshorer, E. *et al.* Hyperdynamic plasticity of chromatin proteins in pluripotent embryonic stem cells. *Dev Cell*
892 **10**, 105-116 (2006). https://doi.org:S1534-5807(05)00421-1 [pii] 10.1016/j.devcel.2005.10.017

893 32 Gaspar-Maia, A., Alajem, A., Meshorer, E. & Ramalho-Santos, M. Open chromatin in pluripotency and
894 reprogramming. *Nature reviews. Molecular cell biology* **12**, 36-47 (2011). https://doi.org:10.1038/nrm3036

895 33 Reynolds, R. C., Montgomery, P. O. & Hughes, B. Nucleolar "Caps" Produced by Actinomycin D. *Cancer Res*
896 **24**, 1269-1277 (1964).

897 34 Holmberg Olausson, K., Nister, M. & Lindstrom, M. S. p53 -Dependent and -Independent Nucleolar Stress
898 Responses. *Cells* **1**, 774-798 (2012). https://doi.org:10.3390/cells1040774

899 35 Rubbi, C. P. & Milner, J. Disruption of the nucleolus mediates stabilization of p53 in response to DNA damage
900 and other stresses. *EMBO J* **22**, 6068-6077 (2003). https://doi.org:10.1093/emboj/cdg579

901 36 Sun, Y. *et al.* MSL2 ensures biallelic gene expression in mammals. *Nature* **624**, 173-181 (2023).
902 https://doi.org:10.1038/s41586-023-06781-3

903 37 Irastorza-Azcarate, I. *et al.* Extensive folding variability between homologous chromosomes in mammalian cells.
904 *bioRxiv* (2024). https://doi.org:10.1101/2024.05.08.591087

905 38 Gribnau, J., Hochedlinger, K., Hata, K., Li, E. & Jaenisch, R. Asynchronous replication timing of imprinted loci
906 is independent of DNA methylation, but consistent with differential subnuclear localization. *Genes Dev* **17**, 759-
907 773 (2003). https://doi.org:10.1101/gad.1059603

908 39 Markowski, J. *et al.* GAMIBHEAR: whole-genome haplotype reconstruction from Genome Architecture Mapping
909 data. *Bioinformatics* **37**, 3128-3135 (2021). https://doi.org:10.1093/bioinformatics/btab238

910 40 Wang, C., Ma, H., Baserga, S. J., Pederson, T. & Huang, S. Nucleolar structure connects with global nuclear
911 organization. *Mol Biol Cell* **34**, ar114 (2023). https://doi.org:10.1091/mbc.E23-02-0062

41 Kefalopoulou, S. *et al.* Time-resolved and multifactorial profiling in single cells resolves the order of heterochromatin formation events during X-chromosome inactivation. *bioRxiv*, 2023.2012.2015.571749 (2023). https://doi.org:10.1101/2023.12.15.571749

42 Berger, A. B. *et al.* High-resolution statistical mapping reveals gene territories in live yeast. *Nat Methods* **5**, 1031-1037 (2008). https://doi.org:10.1038/nmeth.1266

43 Thompson, M., Haeusler, R. A., Good, P. D. & Engelke, D. R. Nucleolar clustering of dispersed tRNA genes. *Science* **302**, 1399-1401 (2003). https://doi.org:10.1126/science.1089814

44 Goronzy, I. N. *et al.* Simultaneous mapping of 3D structure and nascent RNAs argues against nuclear compartments that preclude transcription. *Cell Rep* **41**, 111730 (2022). https://doi.org:10.1016/j.celrep.2022.111730

45 Arrastia, M. V. *et al.* Single-cell measurement of higher-order 3D genome organization with scSPRITE. *Nat Biotechnol* **40**, 64-73 (2022). https://doi.org:10.1038/s41587-021-00998-1

46 Joshi, O. *et al.* Dynamic Reorganization of Extremely Long-Range Promoter-Promoter Interactions between Two States of Pluripotency. *Cell Stem Cell* **17**, 748-757 (2015). https://doi.org:10.1016/j.stem.2015.11.010

47 Langmead, B. & Salzberg, S. L. Fast gapped-read alignment with Bowtie 2. *Nat Methods* **9**, 357-359 (2012). https://doi.org:10.1038/nmeth.1923

48 Danecek, P. *et al.* Twelve years of SAMtools and BCFtools. *Gigascience* **10** (2021). https://doi.org:10.1093/gigascience/giab008

49 Zang, C., Wang, Y. & Peng, W. RECOGNICER: A coarse-graining approach for identifying broad domains from ChIP-seq data. *Quant Biol* **8**, 359-368 (2020). https://doi.org:10.1007/s40484-020-0225-2

50 Ramirez, F., Dundar, F., Diehl, S., Gruning, B. A. & Manke, T. deepTools: a flexible platform for exploring deep-sequencing data. *Nucleic Acids Res* **42**, W187-191 (2014). https://doi.org:10.1093/nar/gku365

51 Krueger, F. & Andrews, S. R. SNPsplit: Allele-specific splitting of alignments between genomes with known SNP genotypes. *F1000Res* **5**, 1479 (2016). https://doi.org:10.12688/f1000research.9037.2

52 Robinson, J. T. *et al.* Integrative genomics viewer. *Nature Biotechnology* (2011). https://doi.org:10.1038/nbt0111-24

53 Andrews, S. FastQC: a quality control tool for high throughput sequence data. (2010).

54 Kopylova, E. N., L.; Touzet, H. SortMeRNA: Fast and accurate filtering of ribosomal RNAs in metatranscriptomic data. *Bioinformatics* (2012).

55 Bolger, A. M., Lohse, M. & Usadel, B. Trimmomatic: a flexible trimmer for Illumina sequence data. *Bioinformatics* **30**, 2114-2120 (2014). https://doi.org:10.1093/bioinformatics/btu170

56 Dobin, A. *et al.* STAR: ultrafast universal RNA-seq aligner. *Bioinformatics* **29**, 15-21 (2013). https://doi.org:10.1093/bioinformatics/bts635

57 Mortazavi, A., Williams, B. A., McCue, K., Schaeffer, L. & Wold, B. Mapping and quantifying mammalian transcriptomes by RNA-Seq. *Nat Methods* **5**, 621-628 (2008). https://doi.org:10.1038/nmeth.1226

58 Consortium, E. R. C. Proposed methods for testing and selecting the ERCC external RNA controls. *BMC Genomics* **6**, 150 (2005). https://doi.org:10.1186/1471-2164-6-150

59 Lerra, L. *et al.* An RNA-dependent and phase-separated active subnuclear compartment safeguards repressive chromatin domains. *Mol Cell* **84**, 1667-1683 e1610 (2024). https://doi.org:10.1016/j.molcel.2024.03.015

60 Sherman, B. T. *et al.* DAVID: a web server for functional enrichment analysis and functional annotation of gene lists (2021 update). *Nucleic Acids Res* **50**, W216-W221 (2022). https://doi.org:10.1093/nar/gkac194

61 Beliveau, B. J. *et al.* Single-molecule super-resolution imaging of chromosomes and in situ haplotype visualization using Oligopaint FISH probes. *Nat Commun* **6**, 7147 (2015). https://doi.org:10.1038/ncomms8147

955 62 Szabo, Q., Cavalli, G. & Bantignies, F. in *Capturing Chromosome Conformation: Methods and Protocols* (eds
956 Beatrice Bodega & Chiara Lanzuolo) 221-237 (Springer US, 2021).

957 63 Marks, H. *et al.* The transcriptional and epigenomic foundations of ground state pluripotency. *Cell* **149**, 590-604
958 (2012). https://doi.org:10.1016/j.cell.2012.03.026

959 64 von Meyenn, F. *et al.* Impairment of DNA Methylation Maintenance Is the Main Cause of Global Demethylation
960 in Naive Embryonic Stem Cells. *Mol Cell* **62**, 848-861 (2016). https://doi.org:10.1016/j.molcel.2016.04.025

961 65 Bonev, B. *et al.* Multiscale 3D Genome Rewiring during Mouse Neural Development. *Cell* **171**, 557-572.e524
962 (2017). https://doi.org:10.1016/j.cell.2017.09.043

963 66 Peric-Hupkes, D. *et al.* Molecular maps of the reorganization of genome-nuclear lamina interactions during
964 differentiation. *Mol Cell* **38**, 603-613 (2010). https://doi.org:S1097-2765(10)00321-7
965 [pii]10.1016/j.molcel.2010.03.016
966

Figure 1

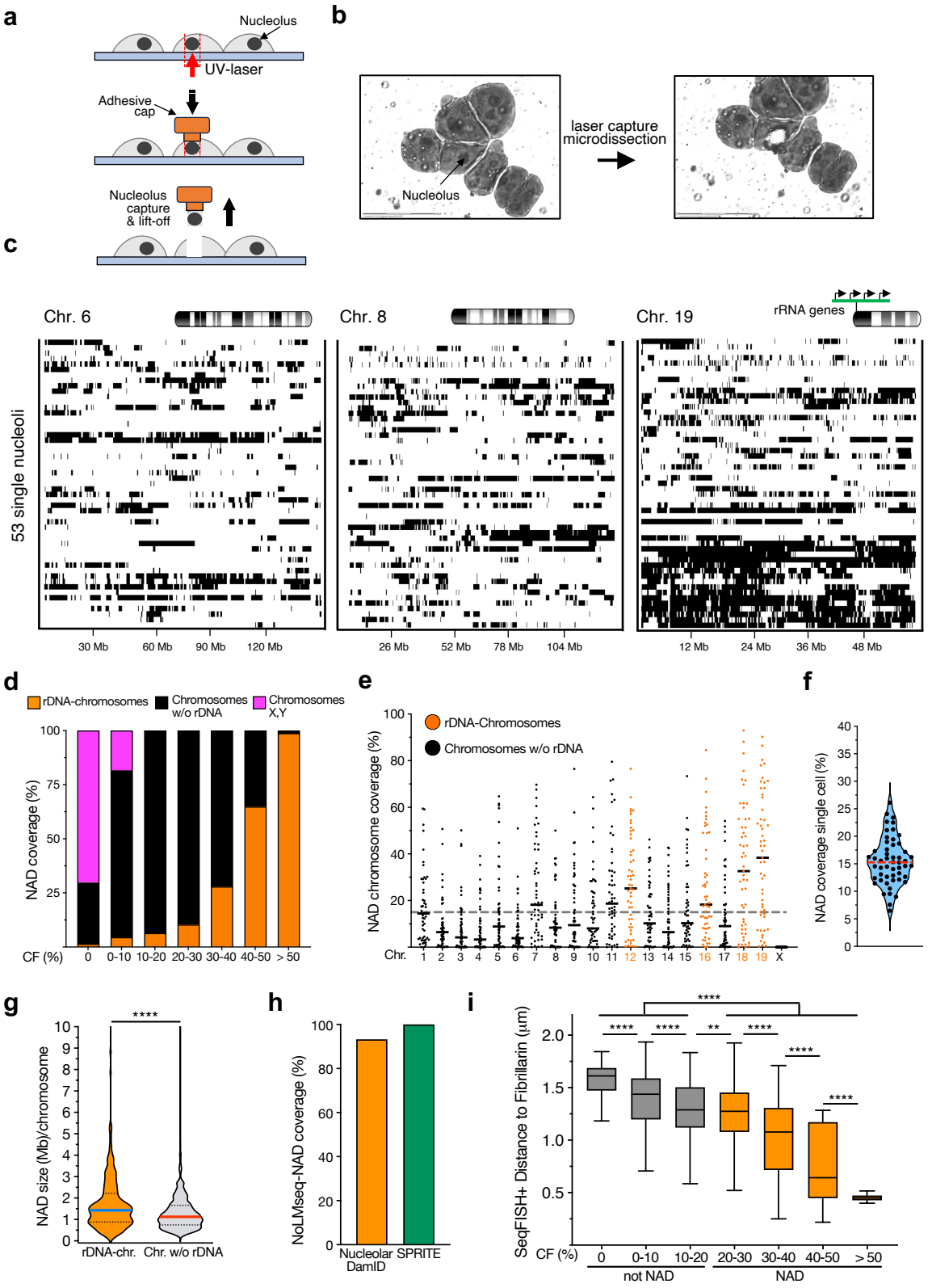
a
Nucleolus
UV-laser
Adhesive cap
Nucleolus capture & lift-off
b
Nucleolus
laser capture microdissection
c
Chr. 6
Chr. 8
Chr. 19
rRNA genes
53 single nucleoli
30 Mb
60 Mb
90 Mb
120 Mb
26 Mb
52 Mb
78 Mb
104 Mb
12 Mb
24 Mb
36 Mb
48 Mb
d
rDNA-chromosomes
Chromosomes w/o rDNA
Chromosomes X,Y
NAD coverage (%)
CF (%)
0
0-10
10-20
20-30
30-40
40-50
> 50
e
rDNA-Chromosomes
Chromosomes w/o rDNA
NAD chromosome coverage (%)
Chr.
f
NAD coverage single cell (%)
g
NAD size (Mb)/chromosome
rDNA-chr.
Chr. w/o rDNA
****
h
NoLMseq-NAD coverage (%)
Nucleolar DamID
SPRITE
i
SeqFISH+ Distance to Fibrillarin (µm)
CF (%)
not NAD
NAD
****
**

Figure 2

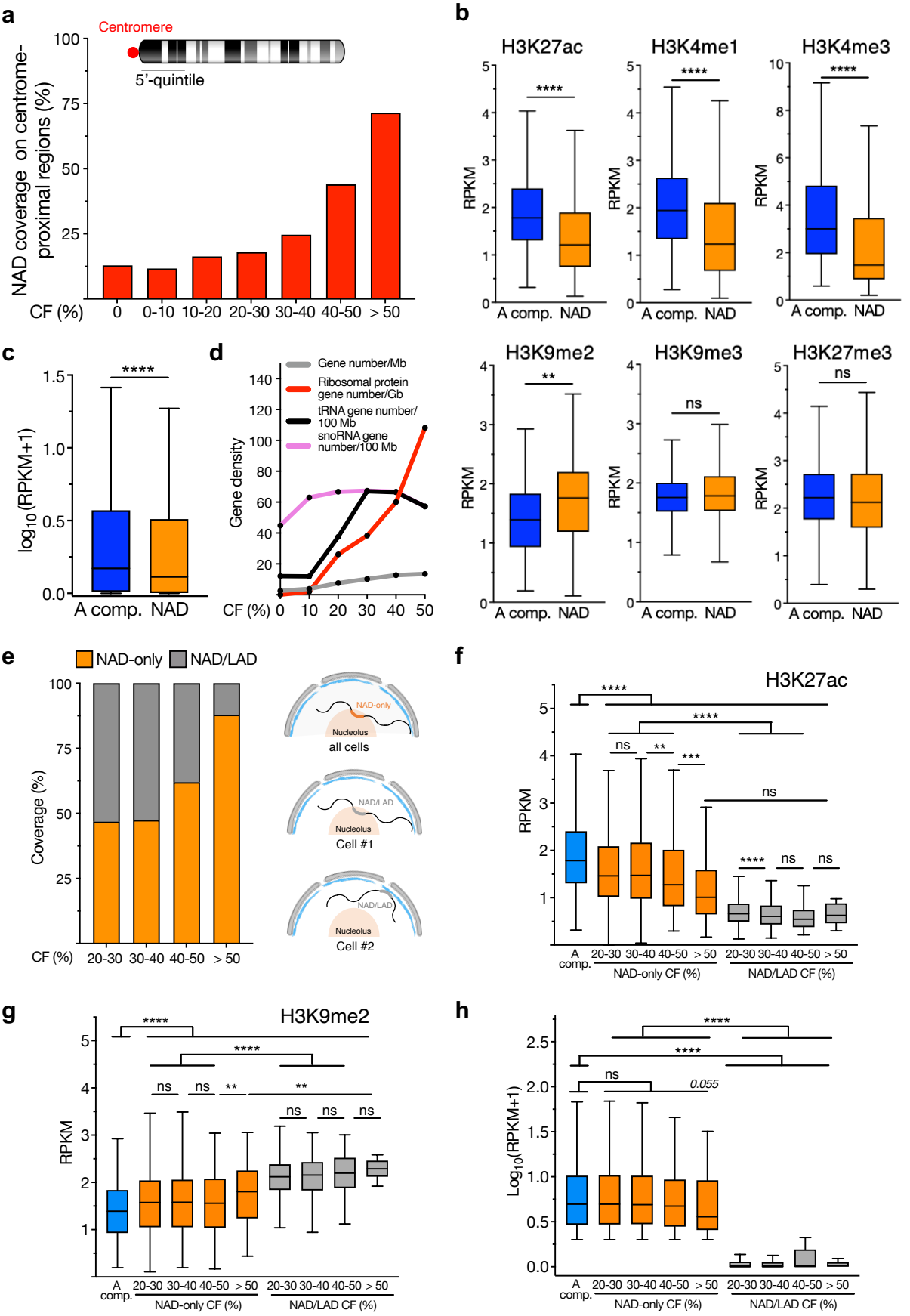
a
Centromere
5'-quintile
NAD coverage on centrome-proximal regions (%)
CF (%)
0
0-10
10-20
20-30
30-40
40-50
> 50
b
H3K27ac
H3K4me1
H3K4me3
RPKM
A comp.
NAD
****
c
log10(RPKM+1)
****
d
Gene number/Mb
Ribosomal protein gene number/Gb
tRNA gene number/ 100 Mb
snoRNA gene number/100 Mb
Gene density
CF (%)
H3K9me2
H3K9me3
H3K27me3
**
ns
e
NAD-only
NAD/LAD
Coverage (%)
CF (%)
20-30
30-40
40-50
> 50
Nucleolus
all cells
Cell #1
Cell #2
f
H3K27ac
A comp.
NAD-only CF (%)
NAD/LAD CF (%)
g
H3K9me2
h
Log10(RPKM+1)
0.055

Figure 3

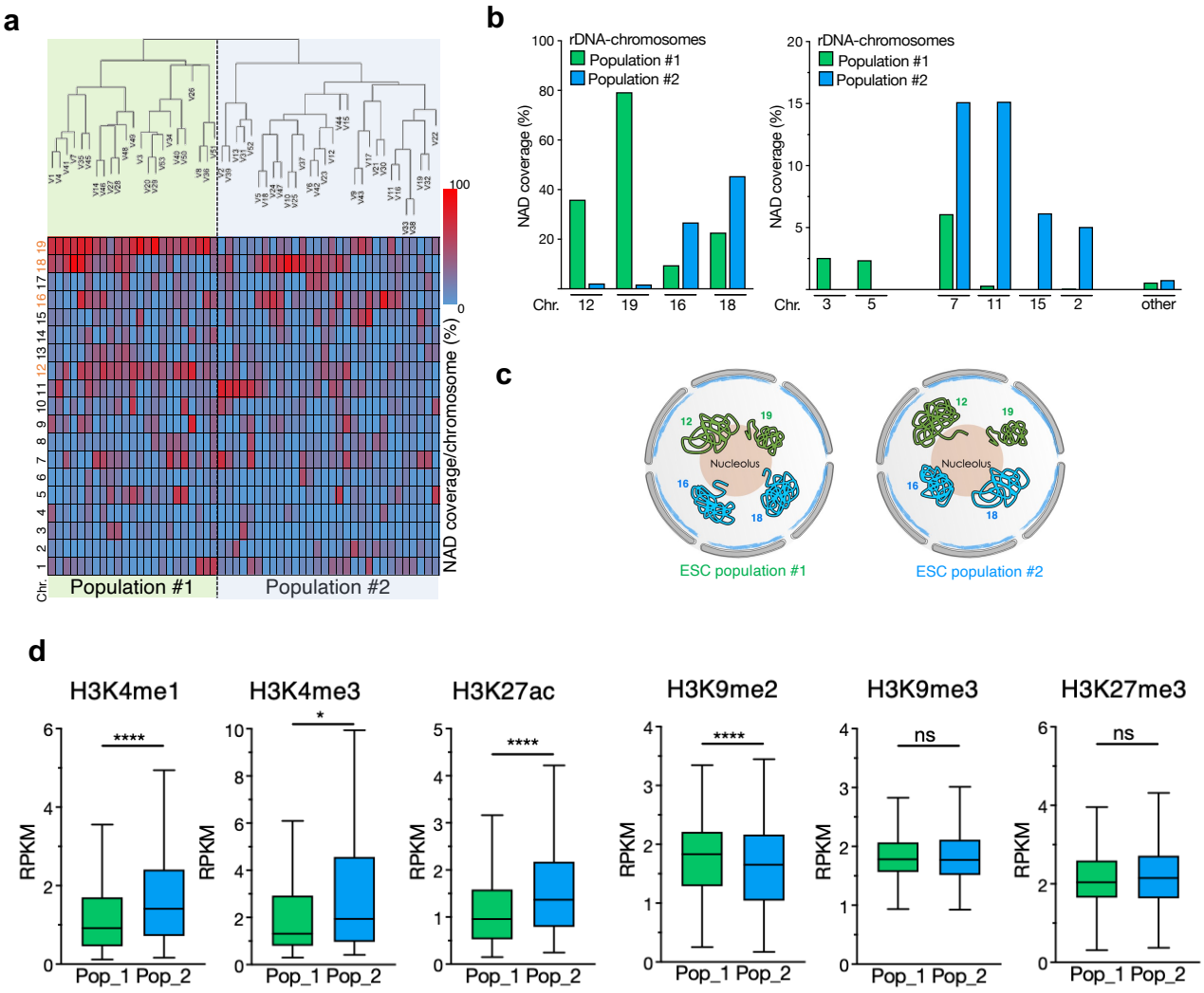
a
Population #1
Population #2
Chr.
NAD coverage/chromosome (%)
b
rDNA-chromosomes
Population #1
Population #2
NAD coverage (%)
Chr.
12
19
16
18
3
5
7
11
15
2
other
c
Nucleolus
ESC population #1
ESC population #2
d
H3K4me1
H3K4me3
H3K27ac
H3K9me2
H3K9me3
H3K27me3
RPKM
Pop_1
Pop_2
****
*
ns

Figure 4

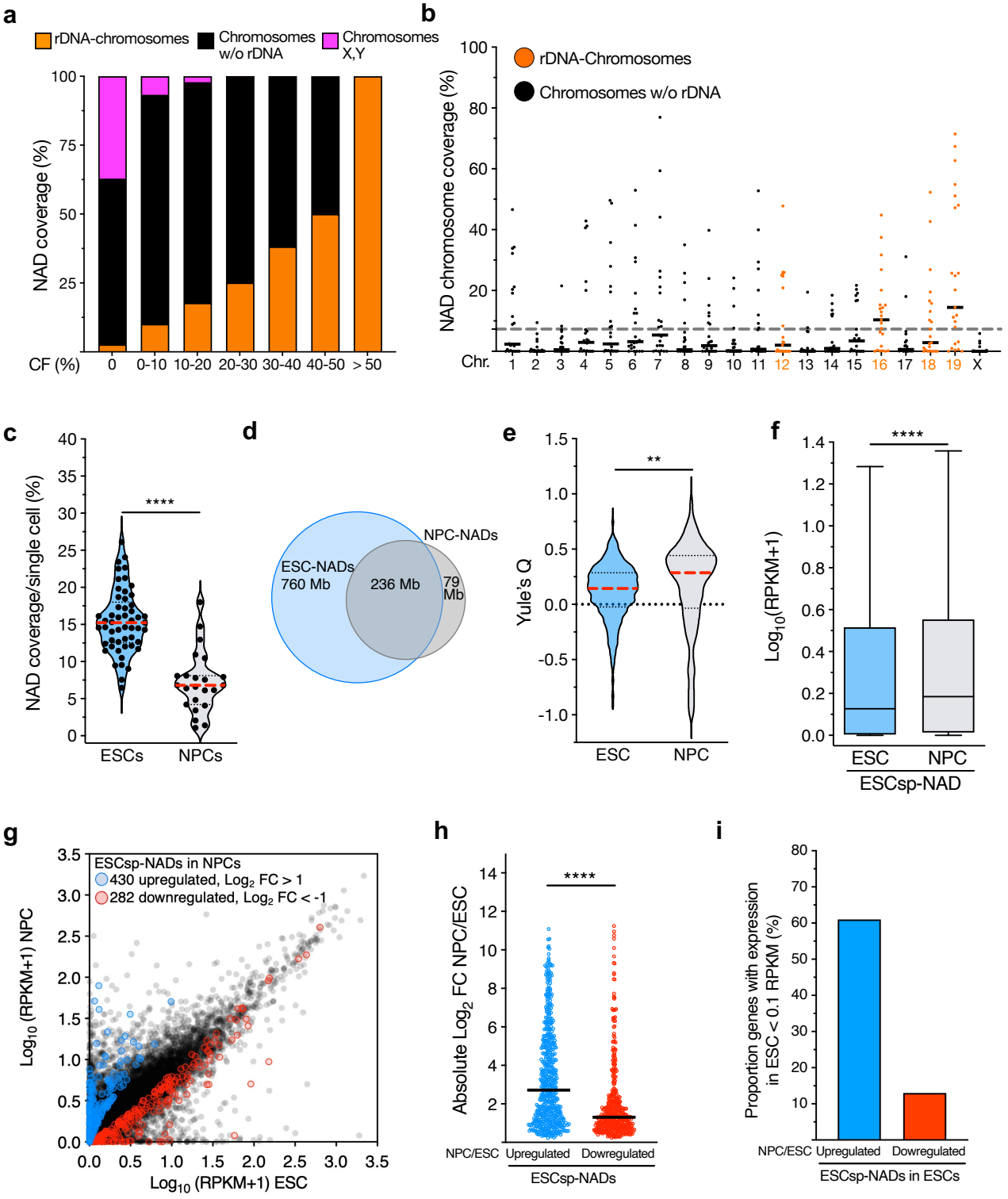
a
rDNA-chromosomes
Chromosomes w/o rDNA
Chromosomes X,Y
NAD coverage (%)
CF (%)
0
0-10
10-20
20-30
30-40
40-50
> 50
b
rDNA-Chromosomes
Chromosomes w/o rDNA
NAD chromosome coverage (%)
Chr.
c
NAD coverage/single cell (%)
****
ESCs
NPCs
d
ESC-NADs
760 Mb
236 Mb
NPC-NADs
79 Mb
e
Yule's Q
**
ESC
NPC
f
Log10(RPKM+1)
****
ESC
NPC
ESCsp-NAD
g
ESCsp-NADs in NPCs
430 upregulated, Log2 FC > 1
282 downregulated, Log2 FC < -1
Log10 (RPKM+1) NPC
Log10 (RPKM+1) ESC
h
Absolute Log2 FC NPC/ESC
****
NPC/ESC
Upregulated
Downregulated
ESCsp-NADs
i
Proportion genes with expression in ESC < 0.1 RPKM (%)
NPC/ESC
Upregulated
Downregulated
ESCsp-NADs in ESCs

Figure 5

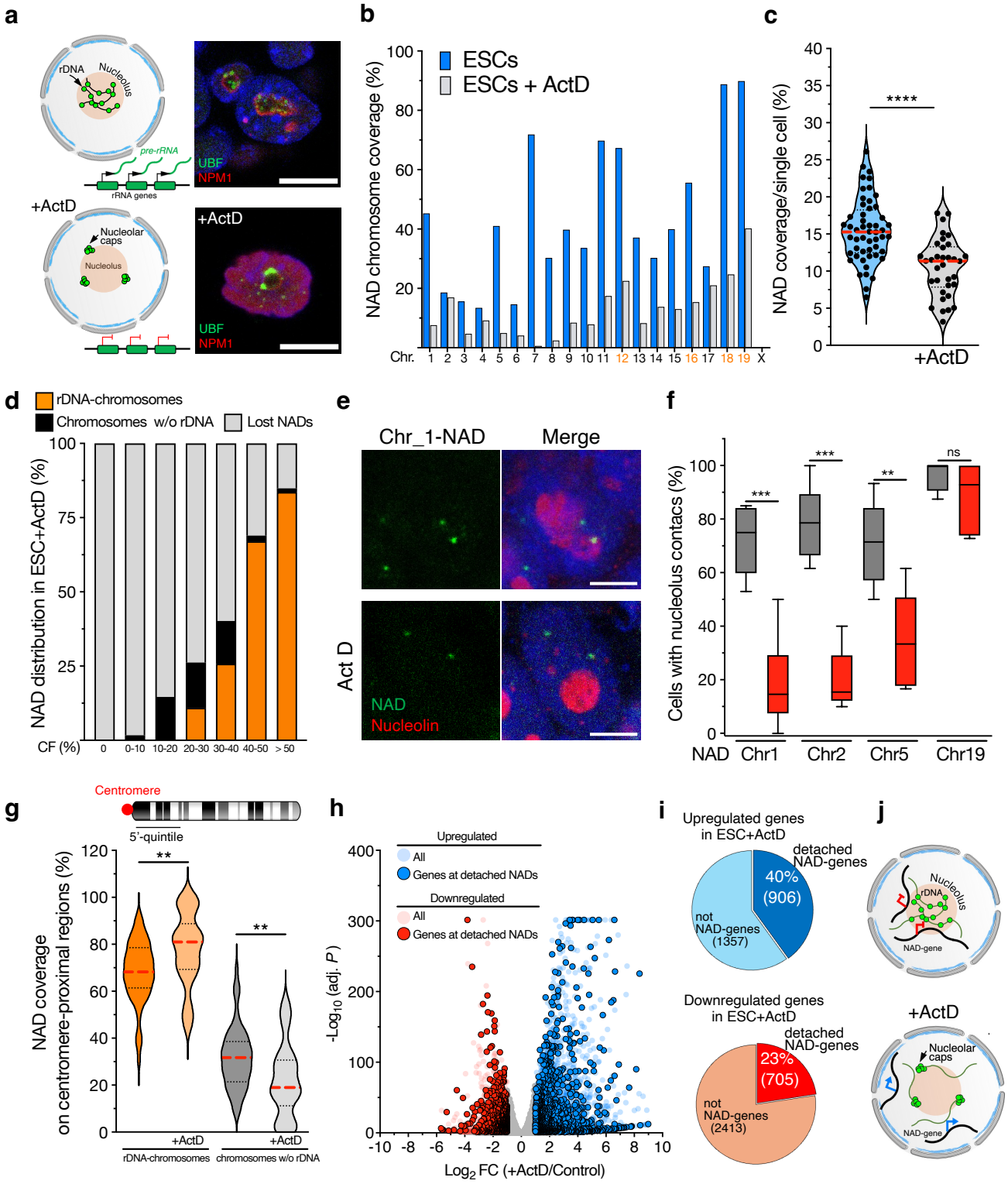
a
rDNA
Nucleolus
pre-rRNA
rRNA genes
UBF
NPM1
+ActD
Nucleolar caps
Nucleolus
+ActD
UBF
NPM1
b
ESCs
ESCs + ActD
NAD chromosome coverage (%)
Chr. 1 2 3 4 5 6 7 8 9 10 11 12 13 14 15 16 17 18 19 X
c
NAD coverage/single cell (%)
****
+ActD
d
rDNA-chromosomes
Chromosomes w/o rDNA
Lost NADs
NAD distribution in ESC+ActD (%)
CF (%) 0 0-10 10-20 20-30 30-40 40-50 > 50
e
Chr_1-NAD
Merge
Act D
NAD
Nucleolin
f
Cells with nucleolus contacs (%)
***
***
**
ns
NAD Chr1 Chr2 Chr5 Chr19
g
Centromere
5'-quintile
NAD coverage on centromere-proximal regions (%)
**
**
+ActD
+ActD
rDNA-chromosomes
chromosomes w/o rDNA
h
Upregulated
All
Genes at detached NADs
Downregulated
All
Genes at detached NADs
-Log10 (adj. P)
Log2 FC (+ActD/Control)
i
Upregulated genes in ESC+ActD
detached NAD-genes
40% (906)
not NAD-genes (1357)
Downregulated genes in ESC+ActD
detached NAD-genes
23% (705)
not NAD-genes (2413)
j
Nucleolus
rDNA
NAD-gene
+ActD
Nucleolar caps
NAD-gene

Figure 6

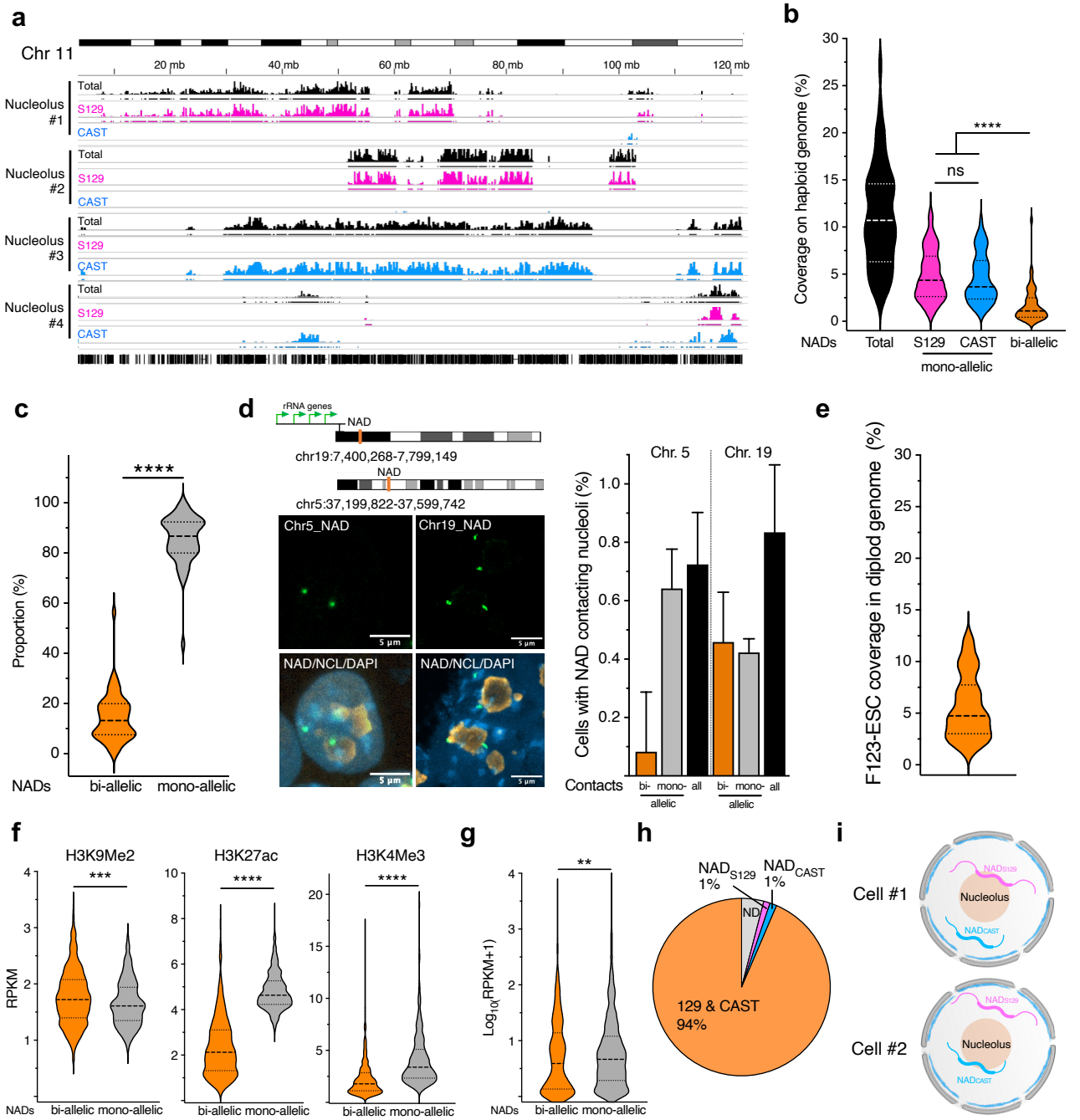
a
Chr 11
20 mb
40 mb
60 mb
80 mb
100 mb
120 mb
Nucleolus #1
Nucleolus #2
Nucleolus #3
Nucleolus #4
Total
S129
CAST
b
Coverage on haploid genome (%)
****
ns
NADs
Total
S129
CAST
bi-allelic
mono-allelic
c
Proportion (%)
****
NADs
bi-allelic
mono-allelic
d
rRNA genes
NAD
chr19:7,400,268-7,799,149
chr5:37,199,822-37,599,742
Chr5_NAD
Chr19_NAD
NAD/NCL/DAPI
NAD/NCL/DAPI
5 µm
Cells with NAD contacting nucleoli (%)
Chr. 5
Chr. 19
Contacts
bi-
mono-
all
allelic
e
F123-ESC coverage in diplod genome (%)
f
H3K9Me2
H3K27ac
H3K4Me3
RPKM
***
****
****
NADs
bi-allelic
mono-allelic
g
Log10(RPKM+1)
**
NADs
bi-allelic
mono-allelic
h
NAD S129 1%
NAD CAST 1%
ND
129 & CAST 94%
i
Cell #1
Cell #2
Nucleolus
NADS129
NADCAST

Figure S1

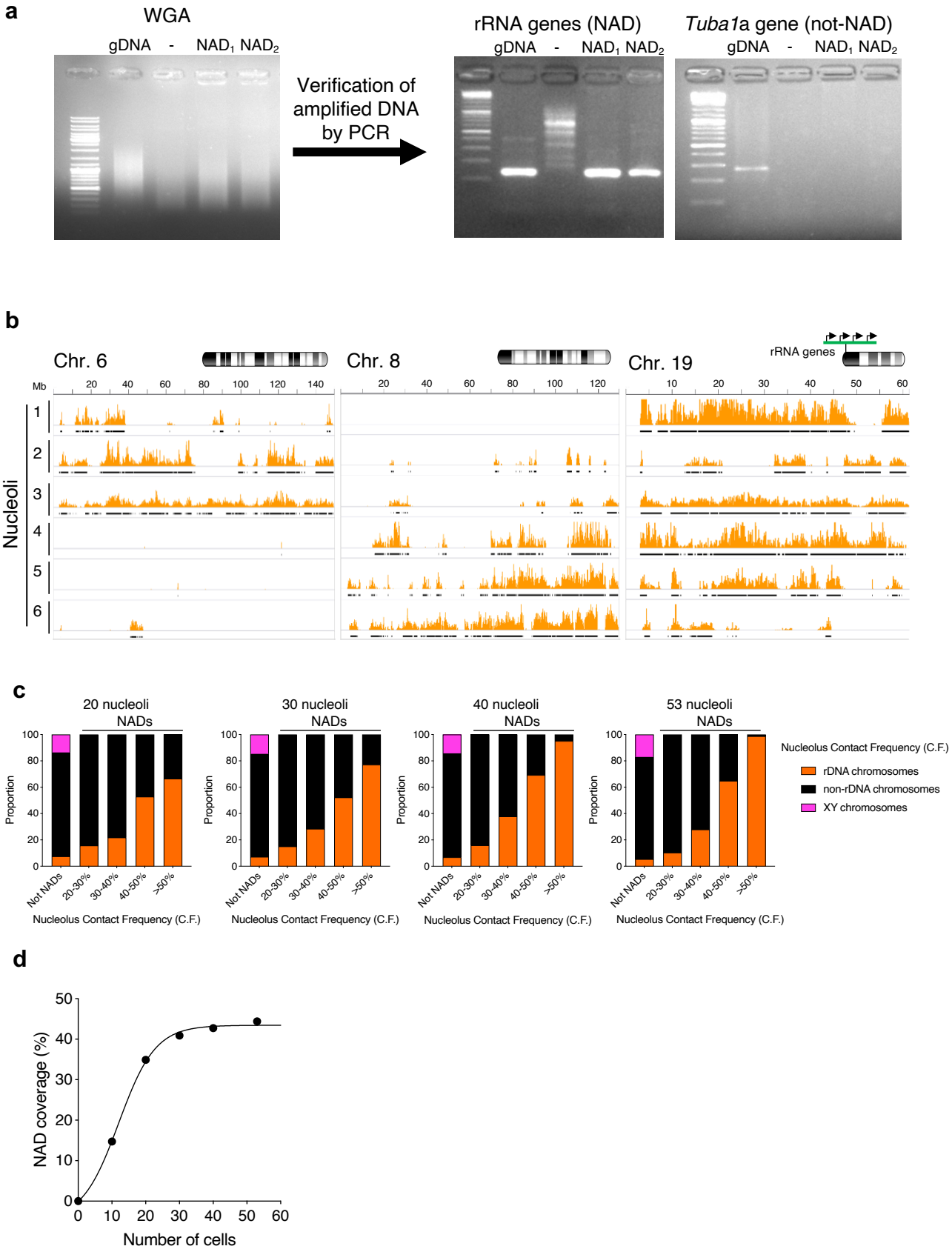
a
WGA
gDNA - NAD1 NAD2
Verification of amplified DNA by PCR
rRNA genes (NAD)
gDNA - NAD1 NAD2
Tuba1a gene (not-NAD)
gDNA - NAD1 NAD2
b
Chr. 6
Chr. 8
Chr. 19
rRNA genes
Mb
Nucleoli
c
20 nucleoli NADs
30 nucleoli NADs
40 nucleoli NADs
53 nucleoli NADs
Proportion
Not NADs
20-30%
30-40%
40-50%
>50%
Nucleolus Contact Frequency (C.F.)
rDNA chromosomes
non-rDNA chromosomes
XY chromosomes
d
NAD coverage (%)
Number of cells

Figure S2

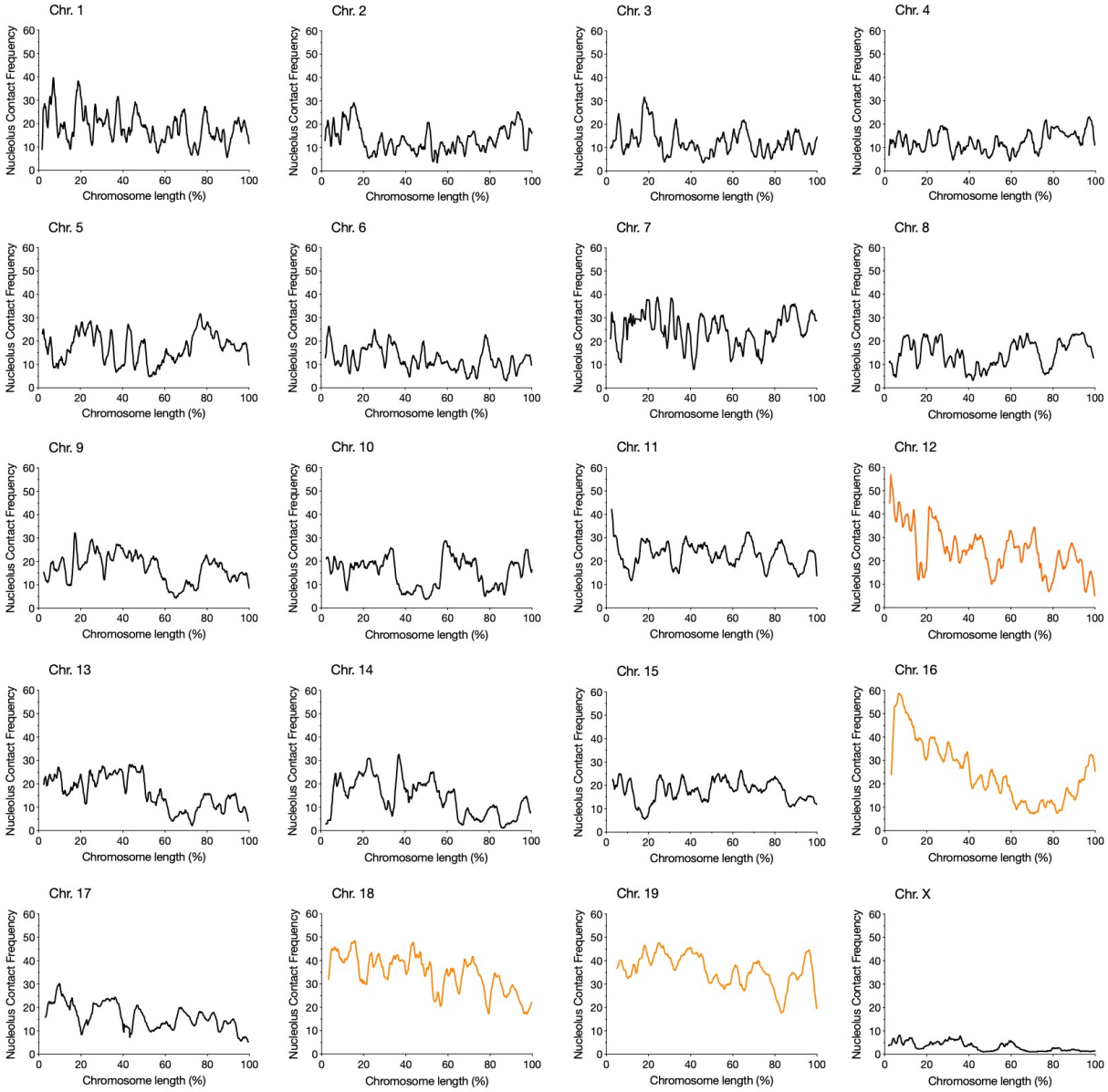
Chr. 1
Chr. 2
Chr. 3
Chr. 4
Chr. 5
Chr. 6
Chr. 7
Chr. 8
Chr. 9
Chr. 10
Chr. 11
Chr. 12
Chr. 13
Chr. 14
Chr. 15
Chr. 16
Chr. 17
Chr. 18
Chr. 19
Chr. X
Nucleolus Contact Frequency
Chromosome length (%)
0
10
20
30
40
50
60
0
20
40
60
80
100

Figure S3

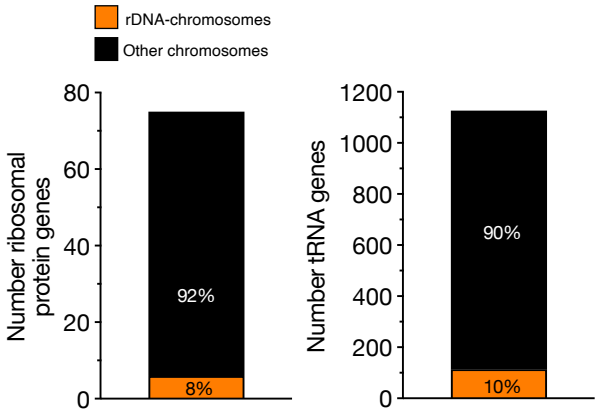
rDNA-chromosomes
Other chromosomes
Number ribosomal protein genes
80
60
40
20
0
92%
8%
Number tRNA genes
1200
1000
800
600
400
200
0
90%
10%

Figure S4

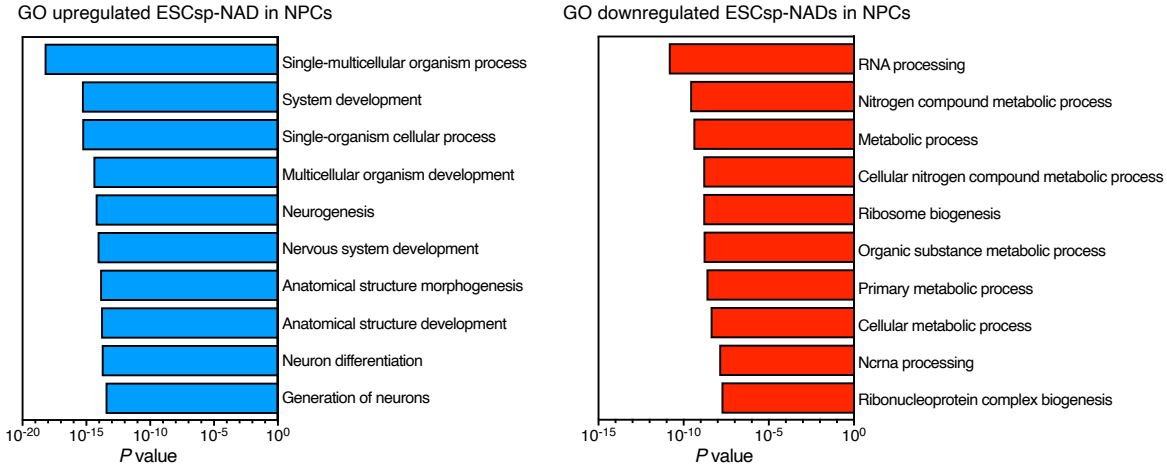
GO upregulated ESCsp-NAD in NPCs
Single-multicellular organism process
System development
Single-organism cellular process
Multicellular organism development
Neurogenesis
Nervous system development
Anatomical structure morphogenesis
Anatomical structure development
Neuron differentiation
Generation of neurons
10-20
10-15
10-10
10-5
100
P value
GO downregulated ESCsp-NADs in NPCs
RNA processing
Nitrogen compound metabolic process
Metabolic process
Cellular nitrogen compound metabolic process
Ribosome biogenesis
Organic substance metabolic process
Primary metabolic process
Cellular metabolic process
Ncrna processing
Ribonucleoprotein complex biogenesis
10-15
10-10
10-5
100
P value

Figure S5

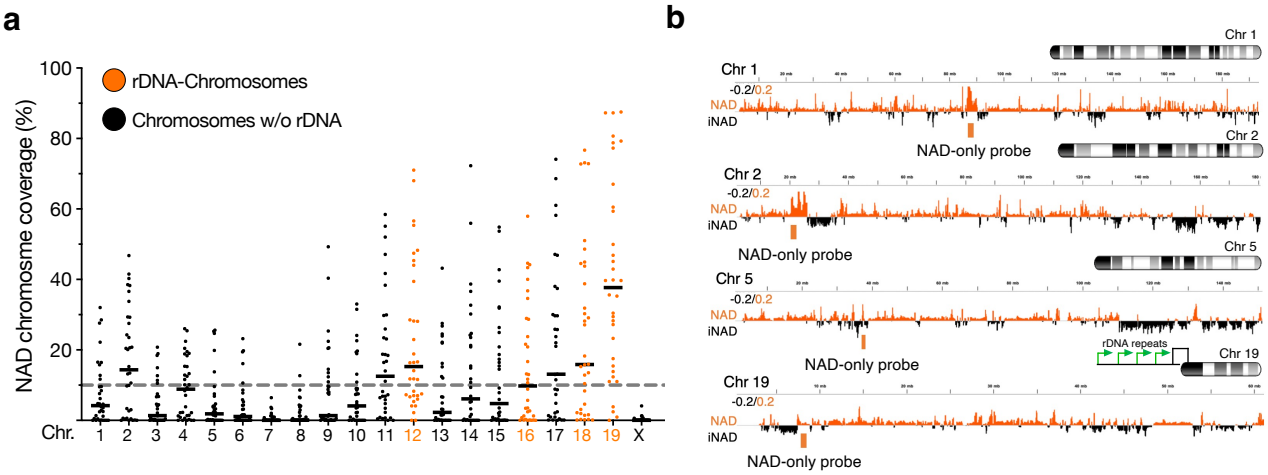
a
rDNA-Chromosomes
Chromosomes w/o rDNA
NAD chromosme coverage (%)
100
80
60
40
20
Chr. 1 2 3 4 5 6 7 8 9 10 11 12 13 14 15 16 17 18 19 X
b
Chr 1
-0.2/0.2
NAD
iNAD
NAD-only probe
Chr 2
Chr 5
Chr 19
rDNA repeats

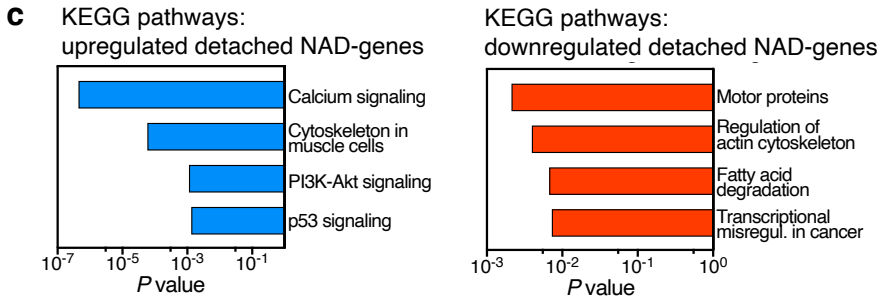
c
KEGG pathways:
upregulated detached NAD-genes
Calcium signaling
Cytoskeleton in muscle cells
PI3K-Akt signaling
p53 signaling
10^{-7} 10^{-5} 10^{-3} 10^{-1}
P value
KEGG pathways:
downregulated detached NAD-genes
Motor proteins
Regulation of actin cytoskeleton
Fatty acid degradation
Transcriptional misregul. in cancer
10^{-3} 10^{-2} 10^{-1} 10^{0}
P value

Figure S6

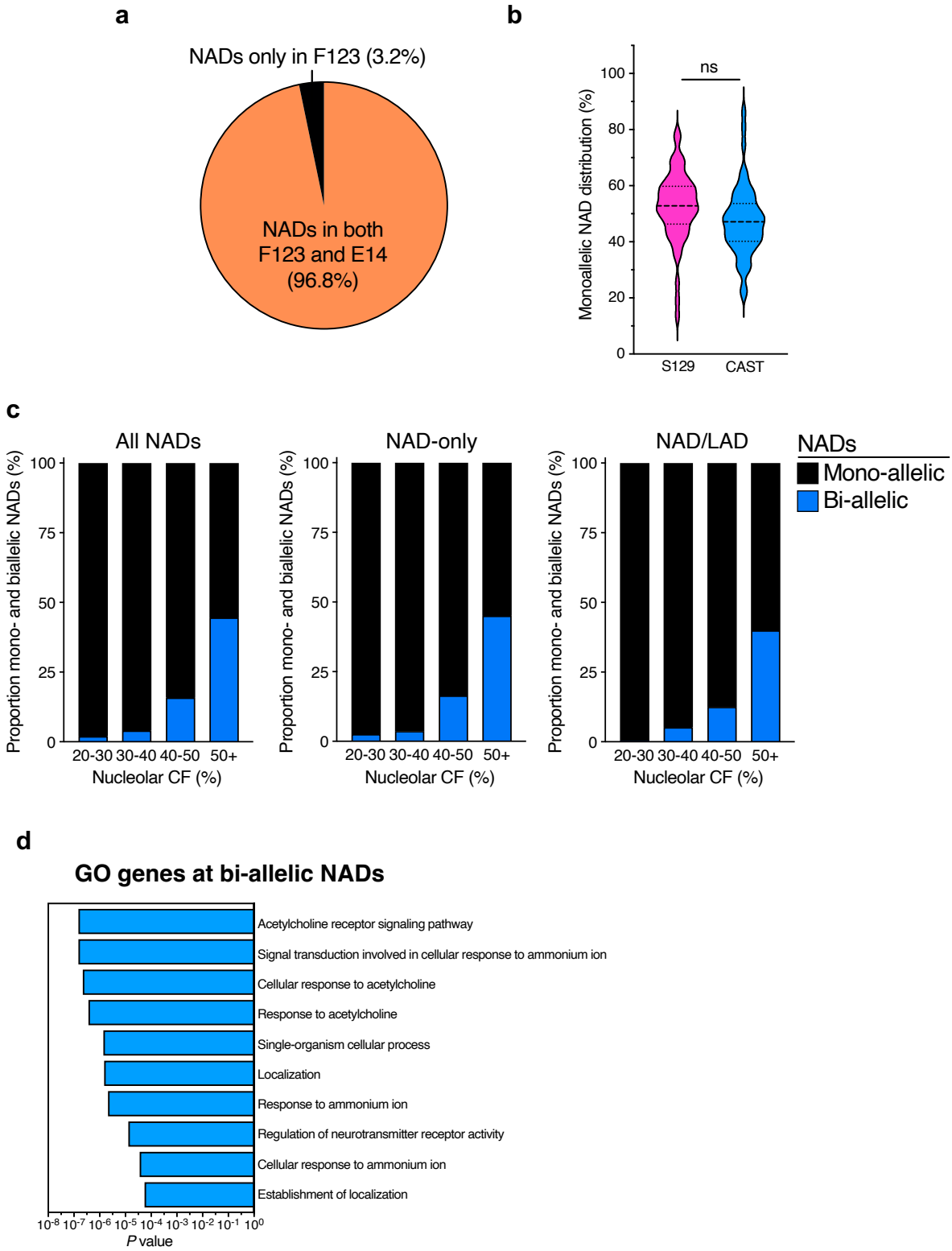
a
NADs only in F123 (3.2%)
NADs in both F123 and E14 (96.8%)
b
ns
Monoallelic NAD distribution (%)
100
80
60
40
20
0
S129
CAST
c
All NADs
NAD-only
NAD/LAD
Proportion mono- and biallelic NADs (%)
100
75
50
25
0
20-30
30-40
40-50
50+
Nucleolar CF (%)
NADs
Mono-allelic
Bi-allelic
d
GO genes at bi-allelic NADs
Acetylcholine receptor signaling pathway
Signal transduction involved in cellular response to ammonium ion
Cellular response to acetylcholine
Response to acetylcholine
Single-organism cellular process
Localization
Response to ammonium ion
Regulation of neurotransmitter receptor activity
Cellular response to ammonium ion
Establishment of localization
10^{-8} 10^{-7} 10^{-6} 10^{-5} 10^{-4} 10^{-3} 10^{-2} 10^{-1} 10^{0}
P value